University of Zurich[UZH]

The composition of Uranus predicted by empirical interior models

Master Thesis in Physics

Sara Engeli

Supervised by
Prof. Dr. Ravit Helled
Dr. Simon Müller

January 25, 2024

Abstract

Understanding the internal structure of Uranus remains a challenge due to the limited data available. The measured parameters are insufficient to arrive at a unique solution for the planet's composition and temperature profiles. This thesis introduces an approach utilizing a random walk algorithm to derive temperature and composition models for Uranus based on a density profile. The random walk algorithm creates random, monotonic temperature profiles and according compositions that fit the given density profile. It starts at the surface and picks matching temperatures and compositions with the algorithm moving towards the center. The algorithm is applied for density profiles from different sources. Some sources also provide according temperature profiles for the density profiles. For those sources, we compare our temperature solutions to the temperature profiles. The comparison showed that our temperature solutions tend to be higher than the temperature profiles of prior publications. From Luca Morf a higher number of density profiles were provided that we used to find temperature and composition profiles for different temperature gradient limits. The temperature results are used to set limits on the central temperature. Depending on the temperature gradient limit the central temperatures are between $(0.4 - 4) \cdot 10^4$ K for lower gradient limits and between $(1.1-16.5)\cdot 10^4$ K for the highest gradient limit. The temperature results are also used to gain information about the heat transport mechanism in Uranus and they are checked for compatibility with magnetic field generation. The composition profiles are used to derive possible bulk compositions of Uranus. Depending on the temperature gradient limit and the central temperatures different bulk compositions were found. But for all compositions, the total mass fraction of hydrogen-helium was below 0.12. In the investigation of the composition layers, we found that for all profiles the hydrogen-helium mass fraction drops below 0.2 and the water mass fraction has an increase to a value above 0.6 at a radius higher than 0.7 r/R_{Uranus}.

Acknowledgements

I would like to thank Prof. Dr. Ravit Helled for giving me the opportunity to write my thesis in this fascinating field and for the time she spent discussing problems with me. I also would like to thank Dr. Simon Müller who explained to me the theoretical basis needed for this thesis and spent many hours answering my questions and helping with coding issues.

Contents

List of Figures

List of Tables

1 Introduction

1.1 Uranus: Discovery and properties

About 240 years ago in the late 18th century, Uranus was detected by Sir William Herschel. Uranus, the seventh planet from the sun, was also the seventh planet to be detected. The planets closer to the sun namely - Mercury, Venus, Mars, Jupiter and Saturn have all been known since prehistoric times. Those closer planets all appear much brighter in our night sky and are therefore easily visible by eye. That's why it was well possible to identify them before telescopes even existed. In very favorable circumstances Uranus is also visible by eye but even then it is very dim. Another challenge for detecting Uranus is its slow orbital motion. It takes Uranus 2 hours to travel the distance of its diameter, while in the case of the Earth, this takes only about seven minutes. Uranus was observed some times before its detection as a planet but because of his slow orbital motion, Uranus was often mistaken as a Star. When Sir William Herschel detected it, he first reported it as a Comet. Since all other planets have been known since antiquity other planets existing in our solar system weren't expected. Three months after its detection Uranus was acknowledged as a planet and was the first planet that was detected with the aid of a telescope. 60 years later in the mid 19th century unexpected changes in the orbit of Uranus led to the detection of Neptune.

Although many things are known by now about the third largest planet of our solar system there are still many open questions about the nature of Uranus. Uranus is located at 20 AU from the Sun. Together with its outer neighbour Neptune, it represents a unique class of planets in our solar system with some similarities. Uranus and Neptune are both referred to as the "ice giants". Uranus has a mass of about 14.5 $M_\oplus$ (earth masses) and a radius of about 4 $R_\oplus$ (earth radii). Neptune has a mass of about 17 $M_\oplus$ and a radius of almost 4 $R_\oplus$. While their sizes are almost identical, Neptune is heavier than Uranus which means that Neptune is denser than Uranus by $\sim 30\%$ [7]. While their masses and sizes are very similar there are also some noticeable differences. Such as their thermal flux. Uranus has a much lower thermal flux than Neptune. The higher heat flux in Neptune suggests that it is still cooling. The lower heat flux in Uranus could suggest that it formed with a cool initial thermal profile and then cooled down enough such that today it has come to thermal equilibrium with the solar insolation. Another possibility is that there is some kind of thermal boundary layer that is preventing the heat from escaping. There might also be some mechanism, such as layered convection and/or conductive or radiative regions that is preventing the heat from escaping efficiently. All those cases suggest that the thermal profile is non-adiabatic [18].

A special feature of Uranus is its large axial tilt. With an axial tilt of 97.77° Uranus is the only planet in our solar system that turns sideways. This special axial tilt results in seasonal changes completely unlike those of the other planets in our solar system. During its orbital period of 84 Earth years around the sun there is always one pole continuously facing the sun while the other pole faces away. This means that each pole gets around 42 years of continuous sunlight until the orientation of the poles towards the sun is reversed and the pole gets another 42 years of darkness. The equator continuously has a rapid day-night cycle with the sun being very low over the horizon.

Figure 1: An image of Uranus taken by Voyager 2 on Jan. 14, 1986

The gravitational and magnetic field of Uranus were measured by the Voyager 2 mission during a flyby. On January 24, 1986, the Voyager 2 spacecraft came closest to Uranus, reaching a distance of approximately 107,000 km from the planet's center. This distance is roughly equivalent to 4 times the radius of Uranus [22]. Until today the Voyager 2 mission is the only spacecraft that has visited Uranus.

1.2 Magnetic field

The first measurements of Uranus magnetic field were taken by Voyager 2. A quite unexpected result of those measurements was that the dipole axis of the magnetic field is tilted from the rotation axis by 60° as shown in figure 2. Also, the magnetic dipole is shifted from Uranus center toward the rotational south pole.

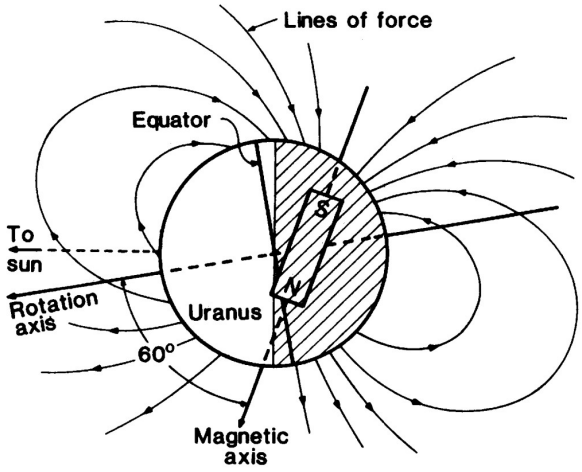

Figure 2: [12]

While the magnetic fields of Jupiter and Saturn are axisymmetric and dipolar, similar to Earth's magnetic field, the measurements of Voyager 2 have shown that Uranus and Neptune

have non-dipolar and non-axisymmetric magnetic fields. The quadrupole (l = 2) and the octupole (l = 3) moments in Uranus and Neptune have comparable power to the dipole (l = 1) moment which means that the field is not dipole-dominated. They also have comparable power in the axisymmetric and the non-axisymmetric components [21]. Since magnetic fields are generated by the motion of a conducting fluid in the interior of a planet, this suggests that there are crucial differences between the interior compositions of Uranus and Neptune and the compositions of Jupiter and Saturn [19].

The hydrogen atmosphere in Uranus and Neptune is much smaller than the one in Jupiter and Saturn and the pressures and temperatures are too low to transform the hydrogen atmosphere into a metallic state. While in Jupiter and Saturn, the large metallic hydrogen region is probably the source region for the dynamo, this isn't possible for Uranus and Neptune. Another possibility for the source region of the dynamo would be a rocky core (that might not even exist). But this is very unlikely because if the field was generated in the deep interior one would expect the magnetic field measured at spacecraft altitude to be dipole-dominated. The reason for this is that one would be much more distant from the source region and the power of the field falls off as r^{2l+4} [21]. Dynamo models from Redmer et al. 2011 suggest that Uranus and Neptune could have fluid shells that extend from about 0.42–0.56 to 0.7–0.8 of the planet's radius. With an ionic water shell extending from 0.6 to 0.8 R_p, in which the conductivity is sufficiently high for sustaining a dynamo process.

1.3 Composition

When we want to explore the composition of Uranus we face some problems. Knowing a planet's mass, radius and some gravitational moments can be used to determine a density distribution that fits the observed parameters but isn't sufficient to get a unique internal density distribution. Even if we would have the internal density distribution we would still need its thermal profile to discover the composition. [18, 17]

Since Uranus and Neptune are known as the "ice giants" one would assume that Uranus should have a high water content. Since Uranus formed far from the Sun in a region where Water condensates, it might be expected that water is prevalent in its composition. However, there is no proof of this assumption. There are even arguments that indicate the opposite. There is evidence that solids in the nearby Kuiper belt have a high rock content [17]. The Kuiper belt lies right outside of Neptune's orbit between about 30 and 50 AU. For objects in the Kuiper belt, a rock to water mass ratio of about 3 was found to fit the compositions [10]. A large rock content can also be observed in the dwarf planet Pluto which also lies in the Kuiper belt. Pluto's measured bulk density directly implies a rock-rich composition. Another argument that could imply a high rock content is modern theories for comets. Comets originate in the outer solar system and there is growing evidence that their rock to water ratio is at least 3 and potentially up to 6. While a high rock to water ratio is expected in the Kuiper belt and comets, in Uranus and Neptune a rock to water ratio of about 0.5 is often expected because this would be consistent with solar composition [17].

1.4 Goal of the thesis

Some fundamental physical properties of Uranus and Neptune are already known. Properties like mass, radius and gravitational field have been measured and can be used to constrain the interiors of these planets. However, the available data is still very limited and therefore the derivation of the interior structure remains a challenge. Uranus and Neptune have so far only been visited by the Voyager 2 spacecraft and many major questions about their origin, evolution

and internal structure remain unsolved. Today we also know that many exoplanets are in the mass and radius range of Uranus and Neptune. There are also smaller versions, so called "mini-Neptunes". Gaining more information about Uranus and Neptune can not only give us a better understanding of those planets but could also be crucial in the understanding of exoplanets [7]. This thesis presents a random walk approach to derive empirical interior models for Uranus. The main goal of this thesis is to get a better understanding of Uranus' composition and derive limitations on its composition and temperature.

The structure of this thesis is as follows. In section 2 some physical properties of Uranus are provided as well as the background theory on the internal structure of planets. Section 2.2 contains the theory on finding density and pressure profiles and provides the information that will be used in the derivation of temperature profiles. The section also explains how properties of mixtures of different materials are derived with the linear mixing approximation (LMA). Additionally, the conditions for the occurrence of a magnetic field dynamo in Uranus are discussed in this section. Section 3 presents the density profiles used in this work to find temperature and composition results with the random walk approach. It also contains temperature profiles from previous work that are used to compare the results found with the random walk approach. This section also explains how the random walk algorithm works. In section 4 the results for different density profiles are shown and discussed. In section 4.1 the temperature results are compared to temperature models of previous work while in section 4.2 the temperature and composition results are presented. For the profile solutions presented in section 4.2, section 4.3 discusses the total bulk compositions and section 4.4 discusses the layers of the composition.

Section 5 will provide a summary of the thesis and its findings, along with a discussion of the directions for future work.

2 Theory

2.1 Physical properties of Uranus

In this section, a summary of the physical properties of Uranus is given.

Parameter	Uranus
semi-major axis (AU)	19.201
mass ($10^{24}kg$)	86.8127 ± 0.0040
mean Radius (km)	25362 ± 7
mean Density (gcm^{-3})	1.270 ± 0.001
$R_{ref}(km)$	25559
$J_2(\times 10^6)$	3510.68 ± 0.70
$J_4(\times 10^6)$	-34.17 ± 1.30
rotation period (Voyager)	$17.24h$
1-bar temperature (K)	76 ± 2
effective temperature (K)	59.1 ± 0.3
intrinsic flux ($Js^{-1}m^{-2}$)	0.042 ± 0.045
bond albedo A	0.30 ± 0.049
axis tilt	$97.77°$

Table 1: Overview of physical properties of Uranus [5]

As already mentioned in section 1.1 the mass of Uranus of about 86.8×10^{24} kg corresponds to roughly 14.5 $M_\oplus$ (earth masses). The radius R_{ref} is the reference equatorial radius with respect to the measured gravitational harmonics J_2 and J_4.

2.2 Internal Structure

The internal Structure of a planet cannot be observed directly but can be approached via theoretical models that fit the planet's observable data such as mass, radius, gravitational field and rotational period.

2.2.1 Density and pressure profiles

If not stated otherwise the information in this section is based on [14]. To find the density profile of a planet two equations are needed. The planets total potential $U(r, \theta)$ consists of the gravitational potential $V(r, \theta)$ and the centrifugal potential $Q(r, \theta)$. The total potential is given by the following equation.

$$\begin{aligned} U(r,\theta) &= V(r,\theta) + Q(r,\theta) \\ &= -\frac{GM}{r}\left(1 - \sum_{n=1}^{\infty}\left(\frac{a}{r}\right)^n J_n P_n(\cos\theta)\right) \\ &\quad + \frac{1}{2}\omega^2 r^2 \sin^2(\theta) \end{aligned} \tag{1}$$

where

r: Distance

θ: Colatitude

G: Gravitational constant

M: Total mass of the planet

a: Equatorial radius at 1 bar

J_n: Gravitational coefficients

P_n: Legendre polynomials

ω: Angular velocity of rotation

For the density profile calculation only even order J values are considered. Since uniform rotation is assumed and dynamics or hemispheric asymmetries are neglected all odd-order J values are equal to zero. The Gravitational coefficients can be calculated by integrating the radial density profile $\rho(r)$ over the planetary volume τ as in the following equation.

$$Ma^n J_n = -\int_\tau \rho(r) r^n P_n(\cos\theta)\, d\tau \tag{2}$$

For Uranus only the low-order gravitational coefficients J_2 and J_4 were measured but have relatively high uncertainties. For higher-order coefficients planetary models are used to predict the J values. A problem in this calculation is that the rotational period of Uranus is not known precisely. And even if all properties were known precisely one would still not find a unique solution for the density profile due to the degenerate nature of this problem.

To find the pressure profile a polytropic equation is used that relates the pressure P to the density ρ.

$$P = K\rho^{1+\frac{1}{n}} \tag{3}$$

where K is the polytropic constant and n is the polytropic index.

2.2.2 Linear Mixing Approximation (LMA)

The materials that are used in this paper to find possible compositions of Uranus are hydrogen, helium, water, rock (i.e. SiO_2) and iron. Water, rock and iron are called heavy elements and their mass fraction is denoted by Z, while hydrogen and helium are denoted by X and Y. The following equations of state (EOS) are used in this thesis. For iron and SiO_2 the QEOS from [11] is used, for water the equation of state from [4] is used. The equation of state for the hydrogen-helium mixture utilizes the CMS from [2], an updated version of SCvH from [20]. The

equations of state include the relation of temperature, pressure, density, internal energy, entropy and adiabatic gradient for the material.

The density of combinations of hydrogen, helium and a heavy element can be calculated as follows.

$$\frac{1}{\rho(P,T)} = \frac{X}{\rho_H(P,T)} + \frac{Y}{\rho_{He}(P,T)} + \frac{Z}{\rho_Z(P,T)} \tag{4}$$

where

X: Mass fraction of hydrogen

Y: Mass fraction of helium

Z: Mass fraction of heavy element

P: Pressure

T: Temperature

The mass fraction is the mass of the material at a certain radius divided by the total mass at this radius. This means that the sum of all mass fractions at a certain radius should be equal to one: $X + Y + Z = 1$. The ratio of the hydrogen and helium mass fraction is taken to be fixed to the solar ratio. The mass fraction of hydrogen and helium in the sun are X = 0.7389 and Y = 0.2463. This leads to a solar ratio of $Y = 0.3333X$.[9]

Equation 4 is known as the linear mixing approximation (LMA) and can also be used more generally for any combinations of N materials [1]. Equation 5 can also be used for combinations of different heavy elements.

$$\frac{1}{\rho(P,T)_{LMA}} = \sum_{i=1}^{N} \frac{X_i}{\rho_i(P,T)} \tag{5}$$

The internal energy for a mixture of N components can be calculated with equation 6 from [1].

$$u(P,T)_{LMA} = \sum_{i=1}^{N} X_i u_i(P,T) \tag{6}$$

The total entropy for a mixture of N components can be calculated with equation 7. For a mixture that contains hydrogen and helium an additional term S_{mix} representing the ideal entropy of mixing gets added to equation 7.

$$S(P,T)_{LMA} = \sum_{i=1}^{N} X_i S_i(P,T) \tag{7}$$

2.2.3 Temperature profile

If not stated otherwise the information in this section is based on [8]. With observations from the outside the inner temperature profile of a planet can't be measured. The only direct information we have about the temperature profile of Uranus is the surface temperature. The surface temperature of Uranus at a pressure of 1 bar is about 76 K [7].

To get an idea of how the inner temperature profile could be found, we have to take a closer look at the energy transport in planets. Energy can be transported by convection, radiation

and conduction. If the energy is transported by convection this leads to an almost adiabatic temperature profile.

Since the thermal flux of Uranus is very low there is either something preventing the interior heat from escaping, like a thermal boundary layer, layered convection, or conductive or radiative regions, or Uranus already formed with a cool interior such that today it has come to thermal equilibrium with the solar insolation. In all those possible cases the heat transport in Uranus can not be overall convective which suggests that the thermal profile is not fully adiabatic [18]. In this work we are only looking at the instantaneous composition and not at its development over time. In some regions, convection that changes the composition could occur. However, convection is a very fast process compared to the lifetime scale of Uranus. Therefore it is very unlikely for large scale convection to happen in regions with changing composition. In this work we therefore don't allow convection in regions with composition changes but only in regions with constant composition. In regions with a homogeneous composition, the heat can be transported by convection or radiation and conduction while in an inhomogeneous region, large scale convection is not allowed. However, even if regular convection is not allowed in an inhomogeneous region the heat transport could still occur via oscillatory double-diffusive convection (usually referred to as semiconvection) [3].

The temperature gradient, meaning the variation of T in the planet with depth, where depth is expressed by the pressure, is defined as follows:

$$\nabla_T := \left(\frac{d\log T}{d\log P}\right) \tag{8}$$

If a planet is in hydrostatic equilibrium and transports the energy by radiation (and conduction) the gradient can be calculated with equation 9.

$$\nabla_{rad} = \frac{3}{16\pi acG}\frac{\kappa l P}{mT^4} \tag{9}$$

where

a:

κ: Mean absorption coefficient

G: Gravitational constant

l: Local luminosity

P: Pressure

m: Mass

T: Temperature

In a homogeneous composition if $\nabla_{rad} < \nabla_{ad}$ the energy is transported by radiation or conduction only and therefore $\nabla_T = \nabla_{rad}$. If $\nabla_{rad} > \nabla_{ad}$ the profile is unstable and convection occurs. The problem with equation 9 is that some properties used in this equation are unknown. The mean absorption coefficient κ depends on the composition and the local thermodynamical conditions which aren't known so far and the local luminosity l is also unknown since we can only measure the thermal flux from the outside and don't know what is in the deeper shells. Since equation 9 can't be solved due to the poorly constrained properties, we need another criterion for stability against large-scale convection.

From [8] we get the criterion that a radiation layer is stable if

$$\nabla_{rad} < \nabla_{ad} + \frac{\phi}{\delta}\nabla_{\mu} \tag{10}$$

with

$$\delta := \left(\frac{\partial \ln \rho}{\partial \ln T}\right), \phi := \left(\frac{\partial \ln \rho}{\partial \ln \mu}\right), \nabla_{\mu} := \left(\frac{d \ln \mu}{d \ln P}\right)_s \tag{11}$$

Equation 10 is known as the Ledoux criterion for dynamical stability. In regions with no changes in the chemical composition, $\nabla_{\mu} = 0$ and we obtain the Schwarzschild criterion for dynamical stability:

$$\nabla_{rad} < \nabla_{ad} \tag{12}$$

If in the criteria 10 and 12 the left side is larger than the right side, the layer is dynamically unstable. If both sides are equal one speaks of marginal stability.

To use the Ledoux criterion the form as in equation 10 not all required quantities are known. To obtain a more practical expression of the Ledoux criterion in this study, equation 13 from [16] is used.

$$\nabla_T < \nabla_{ad} + B \tag{13}$$

with

$$B_k = -\frac{1}{\chi_T}\frac{\ln P(\rho_k, T_k, X_k) - \ln P(\rho_k, T_k, X_{k-1})}{\ln P_k - \ln P_{k-1}} \tag{14}$$

From equation 14 a form as in equation 15 can be derived.

$$B_k = \frac{\chi_\rho}{\chi_T}\frac{\ln \rho(P_k, T_k, C_k) - \ln \rho(P_k, T_k, C_{k-1})}{\ln \rho_k - \ln \rho_{k-1}} \times \frac{\ln \rho_k - \ln \rho_{k-1}}{\ln P_k - \ln P_{k-1}} \tag{15}$$

where P is the pressure, T the temperature, ρ the density, C the composition vector (with the mass fractions of hydrogen, helium, and heavy elements), $\chi_T = \left(\frac{\partial \ln P}{\partial \ln T}\right)_\rho$ and $\chi_\rho = \left(\frac{\partial \ln P}{\partial \ln \rho}\right)_{T,C}$.

In this thesis we use the assumption

$$\chi_\rho = \left(\frac{\partial \ln P}{\partial \ln \rho}\right)_{T,C} \simeq \frac{\ln P_k - \ln P_{k-1}}{\ln \rho_k - \ln \rho_{k-1}} \tag{16}$$

which leads to the simplification

$$B_k = \frac{1}{\chi_T}\frac{\ln \rho(P_k, T_k, C_k) - \ln \rho(P_k, T_k, C_{k-1})}{\ln \rho_k - \ln \rho_{k-1}} \tag{17}$$

This simplification is quite accurate for profiles with almost constant temperatures and compositions but less accurate for rapidly changing temperatures and compositions. Therefore we recommend using equation 14 for future work.

2.2.4 Dynamo region

To be able to create a dynamo there should be a region in Uranus that is convective and contains ionic water at the same time. Therefore solutions that have adiabatic temperature gradients in the ionic water region are particularly interesting. In this work the ionic water region as shown in figure 3 from [19] is used.

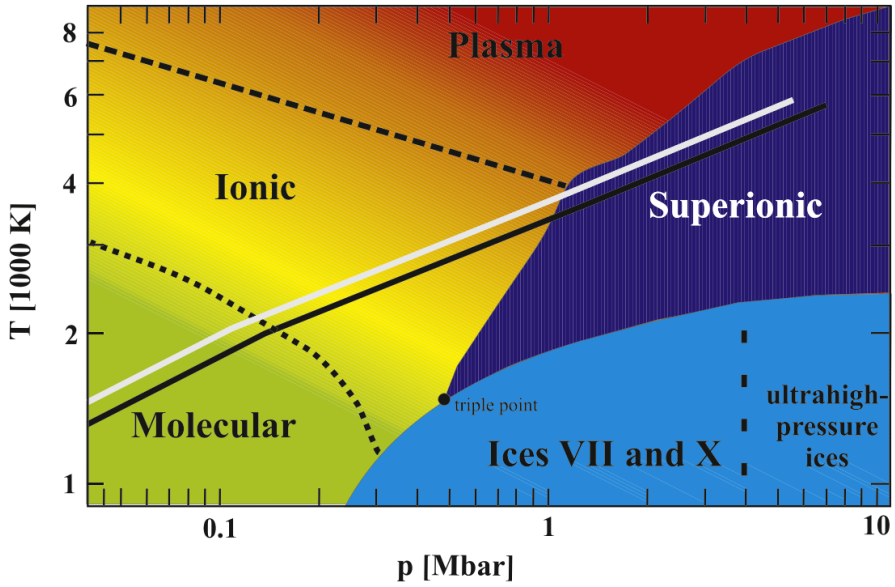

Figure 3: Phase diagram of water up to high pressures as relevant for the interiors of Uranus and Neptune. [19]

The boundaries between the various water phases in figure 3 were only determined within an estimated uncertainty of 10–20%. It is also important to note that the phase diagram shows the ionic region for pure water. However, the interior of Uranus is not necessarily composed of pure water in the pressure and temperature range of the ionic region. Therefore the ionic water region is not completely accurate for compositions with other compounds than water. In the result section the ionic water region will be added to the plots to examine if solutions with adiabatic temperature gradients and water content exist in the ionic water region.

3 Methods

3.1 Uranus density and temperature profiles

For our investigation of Uranus' composition different density profiles were used. Figure 4a shows the density models 1-5 from Neuenschwander et al. 2024 as well as the density models U1 from Nettelmann et al. 2013 and PolyU from Helled et al. 2010. Figure 4b shows the density models from Luca Morf where the color indicates the profile number. Models with higher profile numbers have higher central densities.

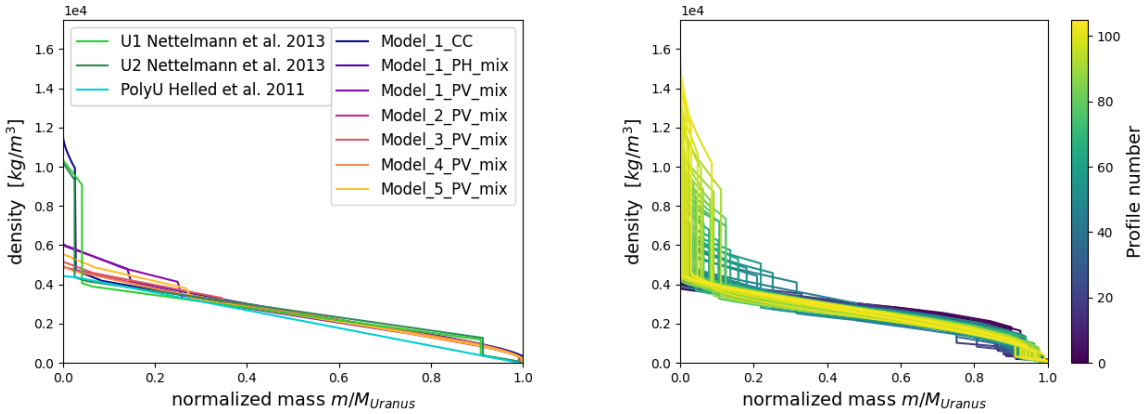

(a) Density profiles model 1 - 5 from [15], U1 and U2 from [13] and PolyU from [6]

(b) Unpublished density profiles provided by Luca Morf

Figure 4: Density models used for the temperature and composition derivation as a function of the normalized mass

Figure 5 shows the temperature models 1-5 from Neuenschwander et al. 2024 as well as the temperature model U1 from Nettelmann et al. 2013 the hot model and the cold model from Podolak et al. 2019. The central temperature models of all those models are within a range of log T = (3.3 - 4.5) K.

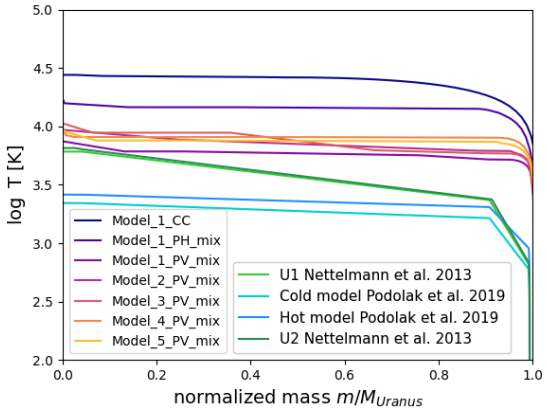

Figure 5: Temperature models used for comparison from [15], [13] and [6] as a function of the normalized mass

3.2 Random Walk

Figure 6 shows a flow chart of the random walk and is followed by an explanation of the random walk algorithm.

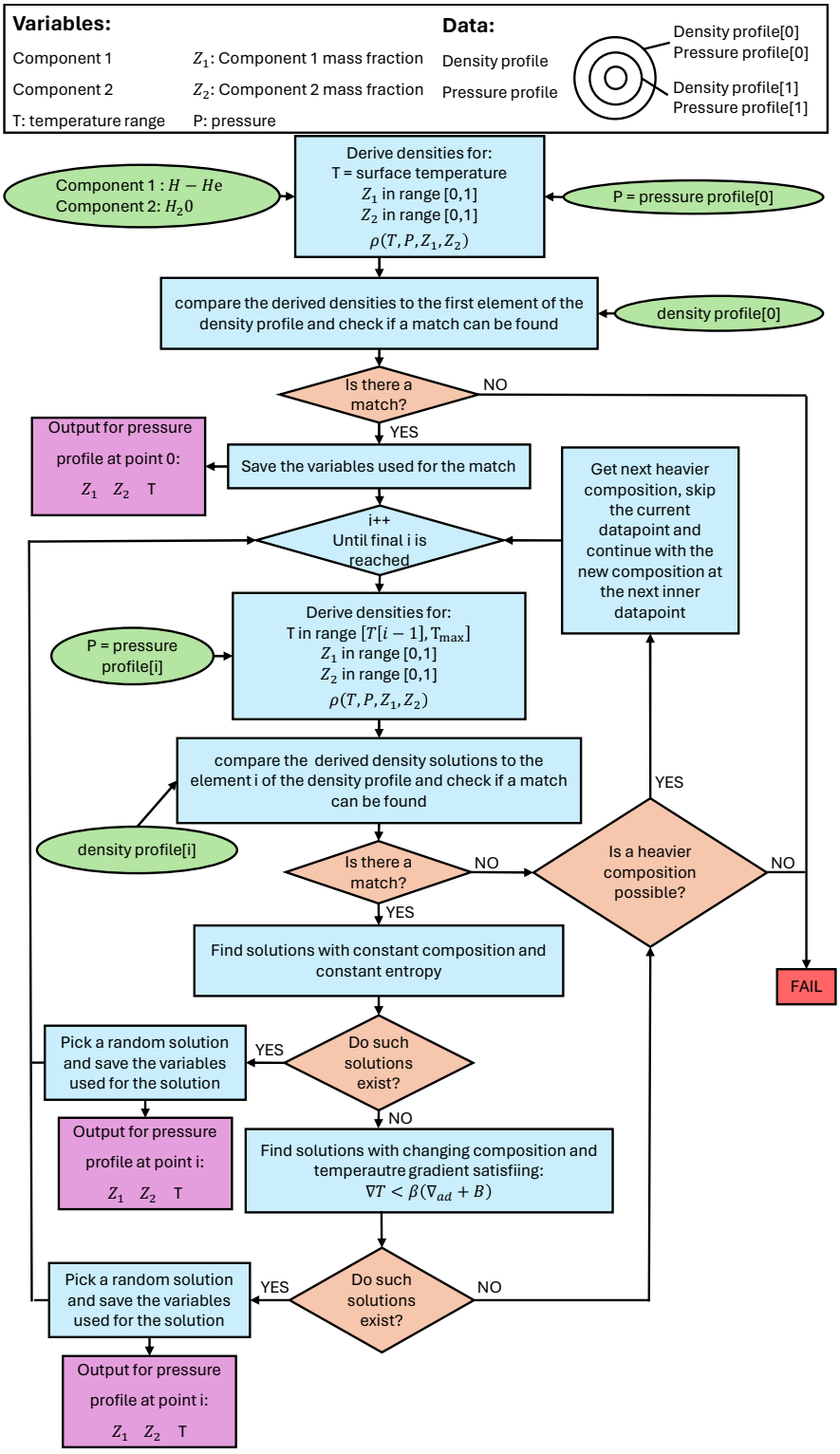

Figure 6: Flow chart for the Random walk algorithm

The Random walk algorithm uses a density and a pressure profile to derive temperature and composition profiles. The composition and temperature profiles are derived with a random walk from outside to inside. For the starting point, two initial components are given. As initial components, we use hydrogen-helium and water. We want to derive the density as a function of the temperature T, the pressure P and the mass fractions Z_1 and Z_2 of the Components 1 and 2. For the pressure, we use the first element of the pressure profile, which, if the pressure profile starts at the surface of the planet, is the surface pressure of 1 bar. If the pressure profile starts at the surface for the temperature we can use the surface temperature of Uranus. For the mass fractions Z_1 and Z_2 all values between 0 and 1 are used in the derivation of the density to get the density solutions for all possible combinations of mass fractions with $Z_1 + Z_2 = 1$. Now we check if one of the derived densities matches the first element of the density profile. If no match is found the random walk fails. If there is a match, the mass fractions Z_1 and Z_2 and the temperature T, used in the density derivation, are saved as the first solution point for the temperature and the composition profiles. The Random walk now continues with the next inner point. For the next inner point again all possible density solutions are derived as a function of T, P, Z_1 and Z_2. For the pressure P, the next element of the pressure profile is taken. For the temperature we now use a range between the previous temperature and a maximal temperature (in this work $T_{max} = 10^{5.5}$ K). For Z_1 and Z_2 again, all values between 0 and 1 are used. Now we check if there are matches between the derived densities and this next inner element of the density profile. If no match can be found the current components are exchanged with the next heavier components and the random walk continues with the next inner point. For example if for the current components we have: Component 1 = $H - He$ and Component 2 = H_2O, then the new components will be: Component 1 = H_2O and Component 2 = SiO_2. If the heaviest elements SiO_2 and Fe were already reached, the component exchange isn't possible and the random walk fails. If density matches can be found, we first take only the solutions with constant compositions with respect to the last point (this constraint is further explained in section 3.2.1) and check if they have a constant entropy (this check is further explained in section 3.2.2). If such solutions exist one of them gets chosen randomly. The mass fractions and the temperature that were used for this solution are saved as the next point in the temperature and composition profile. The random walk will then continue with the next inner point. If no such solution exists we now take only the solutions with changing composition that satisfy the temperature gradient limit $\nabla_T < \beta\,(\nabla_{ad} + B)$. This temperature gradient limit is further explained in section 3.2.3. If such solutions exist one of them gets chosen randomly. The mass fractions and the temperature that were used for this solution are saved as the next point in the temperature and composition profile. The random walk will then continue with the next inner point. If no such solutions exist the current components are exchanged with the next heavier components and the random walk continues with the next inner point. If the heaviest elements SiO_2 and Fe were already reached the component exchange isn't possible and the random walk fails. The random walk ends successfully if the last element of the density and the pressure profile is reached. The last element corresponds to the center of the planet.

3.2.1 Composition constraint

In the search for a solution point, the first attempt is to find a solution with constant composition with respect to the last point. For the solution with constant composition we check if the entropy remains constant which yields an adiabatic temperature profile as presented in section 3.2.2. With this approach, the adiabatic temperature profile is favored whenever the composition is constant. If no constant composition can be found we take a solution with changing composition and check if the temperature of the solution satisfies the the temperature gradient limit presented in section 3.2.3.

Another constraint we give the composition is that the heaviest element in the mixture can only increase.

3.2.2 Entropy constraint

For the solution points with constant composition we check if the entropy from the last to the current solution is also constant. If the entropy is constant the temperature profile is considered to be adiabatic. The entropy is called constant in this work if it satisfies the condition in equation 18.

$$\log S[i+1] - \log S[i] \leq \epsilon \log S[i] \tag{18}$$

3.2.3 Temperature constraint

The first constraint for the temperature is that the temperature has to be monotonically increasing. Going inward this gives us the previous temperature as a minimal value for the temperature range. For computational purposes, an upper limit for the temperature range is needed. The upper limit chosen in this work is T = $10^{5.5}$ K. This upper limit is purposely chosen to be much higher than any value one would expect for the central temperature of Uranus such that this choice does not influence the range of temperature solutions. An additional temperature constraint provides an upper limit for the temperature gradient. Equation 13 is used to limit the temperature gradient. This equation indicates the maximal allowed temperature gradient. However, the gradient limit in reality is probably lower. With temperature gradients allowed as in equation 13 the temperatures in the center sometimes reach very high values. The temperature models used for comparison in this work presented in section 2.2.3 all have central temperatures below 30000 K and to find central temperatures in that range with the random walk algorithm a more restrictive limit for the temperature is needed. Because the temperature limit provided by the Ledoux criterion has a high uncertainty a prefactor $0 < \beta \leq 1$ gets added to equation 13 to find profiles for a diverse range of temperature gradient limits.

$$\nabla_T < \beta \left(\nabla_{ad} + B\right) \tag{19}$$

Equation 19 β describes the relation between the temperature gradient and the Ledoux gradient.

4 Results

In this section, the results for Uranus' temperature and composition profiles with the random walk algorithm are presented. The results are shown for different choices of ϵ in equation 18 for the entropy constraint and for β in equation 19 to limit the temperature gradient. The random walk algorithm was implemented for $\epsilon = 0.01$, 0.001 and $\beta = 1$, 0.5, 0.1. For $\epsilon = 0.001$ in many cases, only very few or no solutions were found while for $\epsilon = 0.01$ it was possible to find solutions for most of the density profiles. Both of those values are very small compared to the uncertainty of the equation of state. For β the values were chosen such that they reflect a range of possible solutions. Also values in between or smaller than the chosen ones could be selected. In section 4.1 the temperature results will be derived for the density profiles shown in figure 4a and compared to previous temperature models shown in figure 5. In section 4.2 the density profiles shown in figure 4b will be used to derive possible solutions for temperature profiles and compositions.

4.1 Comparison of temperature profiles

The temperature results in this part will be derived for the density profiles shown in figure 4a and compared to previous temperature models shown in figure 5. To make the temperatures comparable, the random walk algorithm starts at the same temperature as the temperature model used for the comparison. The composition starts with a combination of hydrogen-helium and water. The plots in this section show the temperature solutions found by the random walk algorithm as well as the temperature model used for comparison. The plots also include the ionic water region shown as a pink area. With a blue background, the plots indicate the regions where at least one of the temperature solutions has an adiabatic gradient (following the condition from section 3.2.2). For some temperature results, we will also show the entropy results which are used in the determination of the adiabatic regions.

4.1.1 Comparison: Part 1

In this section temperature solutions are calculated and compared for a few combinations of density and temperature models. In table 2 the temperature and density profiles used are listed with the figure that shows the according temperature solutions.

Temperature model	Density model	Figure
U1 Nettelmann et al. 2013	U1 Nettelmann et al. 2013	7
U2 Nettelmann et al. 2013	U2 Nettelmann et al. 2013	8
Hot model Podolak et al. 2019	U1 Nettelmann et al. 2013	9
Cold model Podolak et al. 2019	PolyU Helled et al. 2010	10
Hot model Podolak et al. 2019	PolyU Helled et al. 2010	11

Table 2: List of temperature and density models used for comparison

Figure 7 shows the temperature and the entropy solutions for the density model U1 and the temperature model U1 from [13] In figure 7a $\beta = 0.1$ was used for the temperature gradient limit while in figure 7b $\beta = 0.5$ was used. Both cases used $\epsilon = 0.001$. For $\epsilon = 0.01$ no solutions could be found. In the outer part of the planet in the adiabatic region, the solutions match

the temperature model U1. For $\beta = 0.1$ most of the temperature solutions are lower than the temperature model U1. Only towards the center, there is a higher temperature solution. For $\beta = 0.5$, the temperature solutions cover the region of the temperature model U1, however there is no completely matching solution. For $\beta = 1$, there were only very few solutions found that are much higher than the temperature model U1. Figures 7c and 7d show the associated entropy as a function of the normalized radius for the temperature profiles in figures 7a and 7b. The entropy plots show that in a region where at least one of the entropy solutions remains sufficiently constant the region gets labeled as adiabatic.

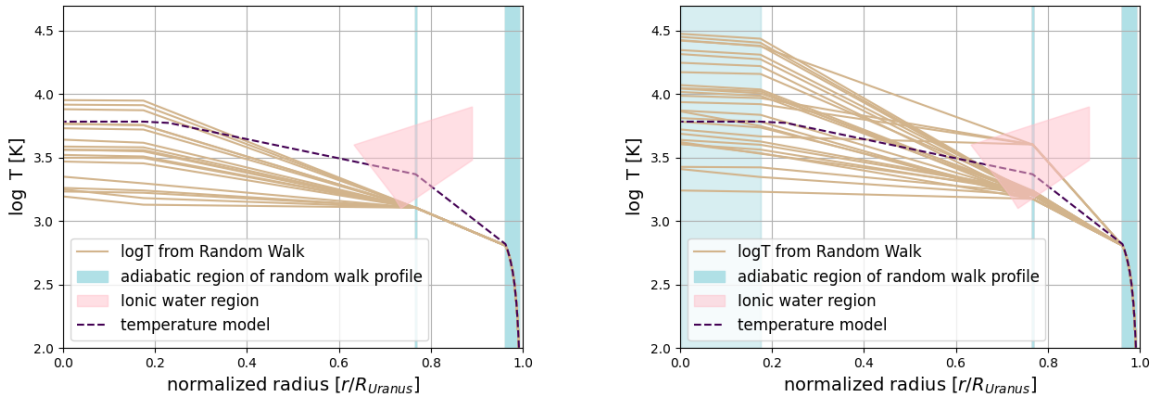

(a) with $\beta = 0.1$ and $\epsilon = 0.001$

(b) with $\beta = 0.5$ and $\epsilon = 0.001$

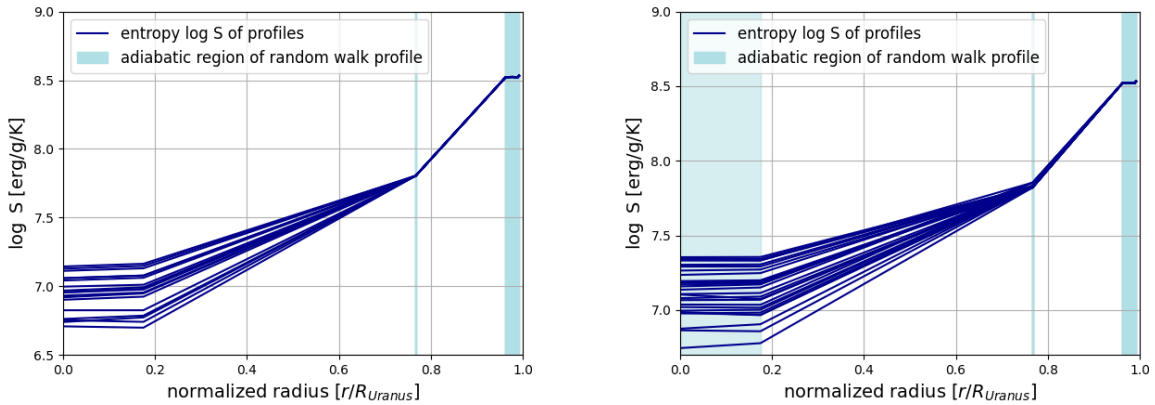

(c) with $\beta = 0.1$ and $\epsilon = 0.001$

(d) with $\beta = 0.5$ and $\epsilon = 0.001$

Figure 7: Temperature and entropy solutions for density model U1 and the temperature model U1 from Nettelmann et al.2013

Figure 8 shows the temperature solutions for the density model U2 and the temperature model U2 from [13]. In figure 8a $\beta = 0.1$ was used for the temperature gradient limit while in figure 8b $\beta = 0.5$ was used. Both cases used $\epsilon = 0.001$. For $\epsilon = 0.01$ no solutions could be found. In the outer part of the planet in the adiabatic region, the solutions match the temperature model U2. For $\beta = 0.1$ most of the temperature solutions are lower than the temperature model U2. Only towards the center, there is a higher temperature solution. For $\beta = 0.5$, the temperature solutions completely cover the region of the temperature model U2. For $\beta = 1$, no solutions were found.

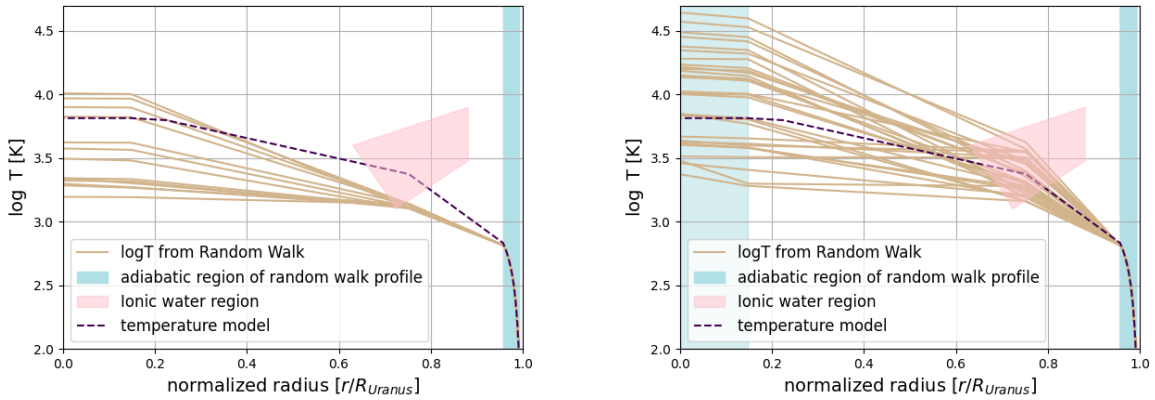

(a) with $\beta = 0.1$ and $\epsilon = 0.001$ (b) with $\beta = 0.5$ and $\epsilon = 0.001$

Figure 8: Temperature solutions for density model U2 and the temperature model U2 from Nettelmann et al.2013

Figure 9 shows the temperature solutions for the density model U1 from [13] and the hot temperature model from [18]. In figure 9a $\beta = 0.1$ was used for the temperature gradient limit while in figure 9b $\beta = 0.5$ was used. Both cases used $\epsilon = 0.001$. For $\epsilon = 0.01$ no solutions could be found. In the outer part of the planet in the adiabatic region, the solutions match the hot temperature model. For $\beta = 0.1$ in the outer part, the temperature solutions are lower than the hot temperature model while towards the center they cover the same region. For $\beta = 0.5$ the temperature solutions cover the region of the hot temperature model for the majority of the planet's radius, however, the central temperature solutions are all higher than the hot temperature model. For $\beta = 1$, no solutions were found.

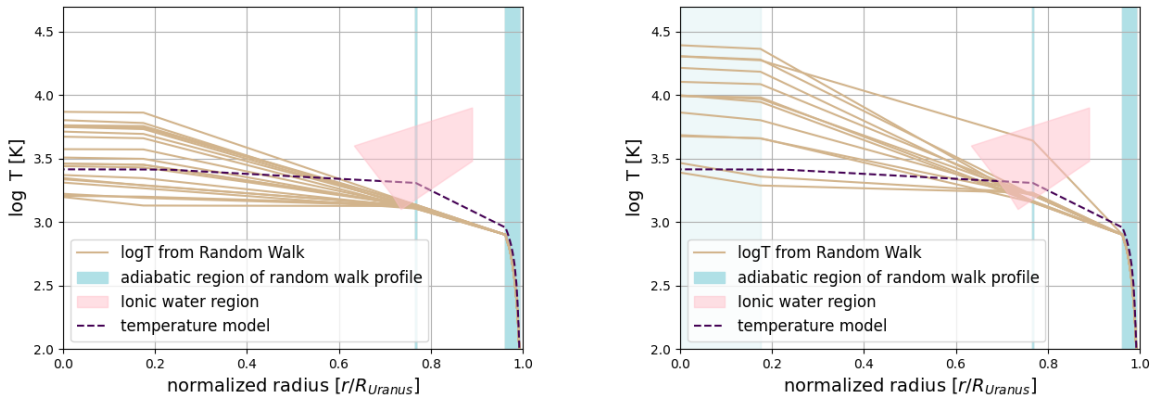

(a) with $\beta = 0.1$ and $\epsilon = 0.001$ (b) with $\beta = 0.5$ and $\epsilon = 0.001$

Figure 9: Temperature solutions for density model U1 from Nettelmann et al.2013 and the hot temperature model from Podolak et al.2019

Figure 10 shows the temperature solutions for the density model PolyU from [6] and the cold temperature model from [18]. In figure 10a $\beta = 0.1$ was used for the temperature gradient limit while in figure 10b $\beta = 1$ was used. Both cases used $\epsilon = 0.01$. For $\beta = 0.1$, all temperature solutions are higher than the cold temperature model for the whole planet, even in the adiabatic region. For $\beta = 1$, the temperature solutions are all higher than the cold temperature model in

the outer part and the center. In between the temperature solutions cover the region of the cold temperature model. For $\beta = 0.5$, the solutions look almost identical to the solutions for $\beta = 1$. For $\epsilon = 0.001$, the temperature solutions are even higher than in the examples shown here.

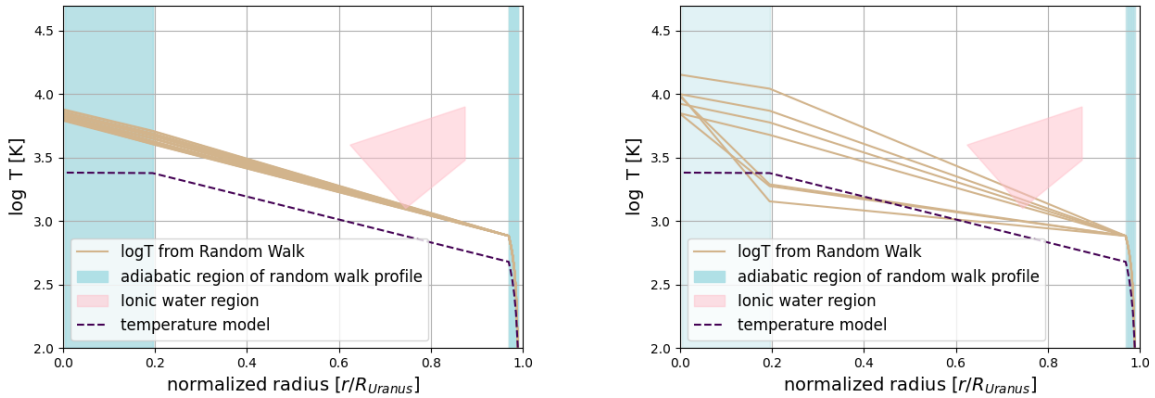

(a) with $\beta = 0.1$ and $\epsilon = 0.01$ (b) with $\beta = 1$ and $\epsilon = 0.01$

Figure 10: Temperature solutions for density model PolyU from Helled et al.2010 and the cold temperature model from Podolak et al.2019

Figure 11 shows the temperature solutions for the density model PolyU from [6] and the hot temperature model from [18]. In figure 11a $\beta = 0.1$ was used for the temperature gradient limit while in figure 11b $\beta = 1$ was used. Both cases used $\epsilon = 0.01$. In the outer part in the adiabatic region, all temperature solutions match the hot temperature model. For $\beta = 0.1$, all temperature solutions are higher than the hot temperature model for the majority of the planet's radial range. For $\beta = 1$, the temperature solution matches the hot temperature model for a majority of the planet's radial range, only towards the center all temperature solutions are higher. For $\beta = 0.5$, the solutions look almost identical to those for $\beta = 1$. For $\epsilon = 0.001$, the temperature solutions are higher than in the examples shown here.

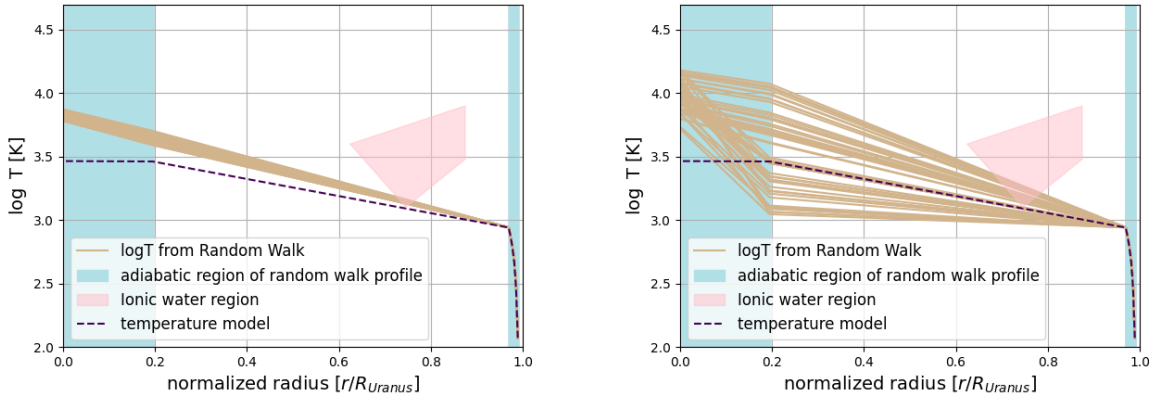

(a) with $\beta = 0.1$ and $\epsilon = 0.01$ (b) with $\beta = 1$ and $\epsilon = 0.01$

Figure 11: Temperature solutions for density model PolyU from Helled et al.2010 and the hot temperature model from Podolak et al.2019

The figures in this section show that the choice of β and ϵ can have a great impact on the

number of solutions found and the compatibility of the temperature solutions and the temperature models. However, some conclusions are independent of the choice of β and ϵ. For the cold model from Podolak et al. 2019 the central temperatures of the model are always smaller than the temperature solutions. For a combination of the cold model and the density model U1 from Nettelmann et al. 2013 no solutions were found. For the hot model from Podolak et al. 2019 the central temperatures are also smaller than the temperature solutions in many cases. Only for a small β value of 0.1, temperature solutions with the same central temperature as the hot model were found. The best temperature fit was found for the density and temperature models U1 and U2 from Nettelmann et al. 2013. For both cases β needs to be smaller than 1 to find solutions but for a suitable choice of β the temperature models are both well within the range of temperature solutions at any radius. Since we expect β to be smaller than 1 and possibly even significantly smaller these results agree with our expectations on the temperature gradient limit presented in section 3.2.3.

4.1.2 Comparison: Part 2

In this section temperature solutions and the compositions are calculated and compared for different profiles from [15]. For the density profiles in this section, the random walk algorithm fails to get solutions in the outer part of the planet when pressures are below 1000 bar. Consequently, all profiles in this section start at a pressure of 1000 bar, beginning with the temperature value corresponding to the temperature models at this pressure.

Figure 12 shows the temperature solutions for the density and the temperature model 1 CC from [15]. In figure 12a $\beta = 0.1$ was used for the temperature gradient limit while in figure 12b $\beta = 0.5$ and in figure 12c $\beta = 1$ was used. All of those cases use $\epsilon = 0.01$. In the outer part, there is a region where all temperature solutions are aligned with the 1 CC temperature model. This region is also adiabatic. For $\beta = 0.1$, all temperature solutions are lower than the 1 CC temperature model except for the outer part. For $\beta = 0.5$ in the middle part temperature solutions are lower and towards the center cover the region of the 1 CC temperature model. For $\beta = 1$ in the outer part, the temperature solutions are lower and towards the center, they are higher than the 1 CC temperature model. For $\epsilon = 0.001$ no temperature solutions were found.

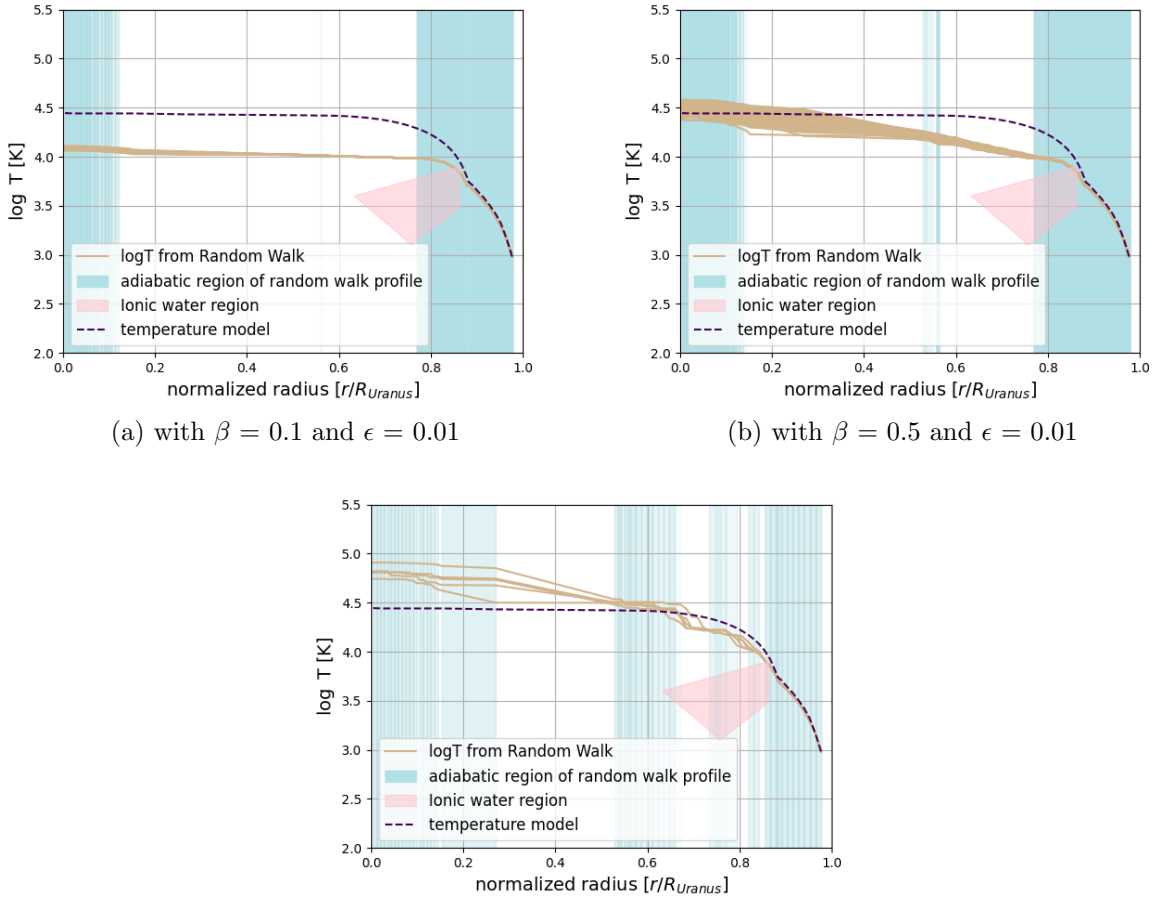

(a) with $\beta = 0.1$ and $\epsilon = 0.01$

(b) with $\beta = 0.5$ and $\epsilon = 0.01$

(c) with $\beta = 1$ and $\epsilon = 0.01$

Figure 12: Temperature solutions for density and temperature model 1 CC from [15]

Figure 13 shows the temperature solutions for the density and the temperature model 1 PH from [15]. In figure 13a $\beta = 0.5$ was used for the temperature gradient limit while in figure 13b $\beta = 1$ was used. Both cases use $\epsilon = 0.01$. In the outer part, there is a small region

where all temperature solutions are aligned with the 1 PH temperature model. This region is also adiabatic. For $\beta = 0.5$ in most of the outer part the temperature solutions are lower and towards the center cover the region of the 1 PH temperature model. For $\beta = 1$ in the outer part, the temperature solutions are lower and towards the center, they are higher than the 1 PH temperature model. For $\epsilon = 0.001$ no temperature solutions were found.

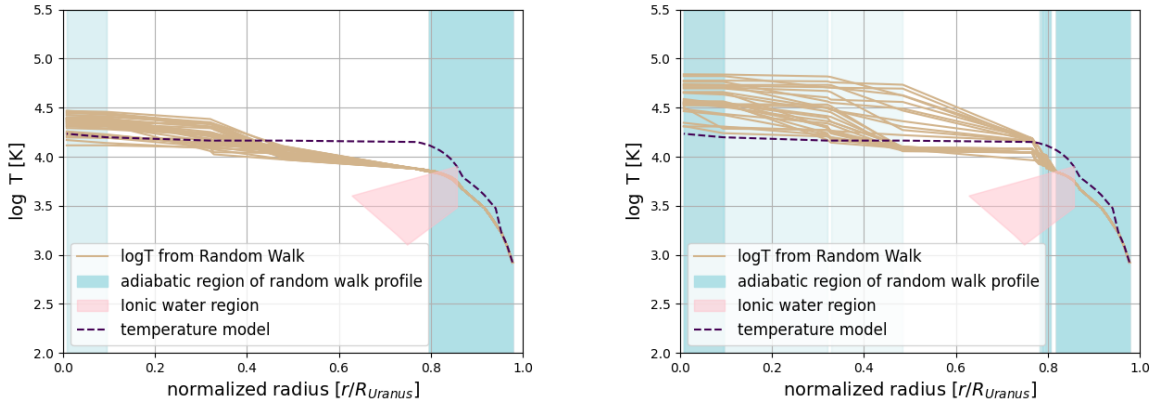

(a) with $\beta = 0.5$ and $\epsilon = 0.01$ (b) with $\beta = 1$ and $\epsilon = 0.01$

Figure 13: Temperature solutions for density and temperature model 1 PH from [15]

Figure 14 shows the temperature solutions for the density and the temperature model 1 PV from [15]. In figure 14a $\epsilon = 0.01$ was used for the entropy constraint while in figure 14b $\epsilon = 0.001$ was used. Both cases use $\beta = 1$. For the smaller β values 0.5 and 0.1 no solutions were found. For $\epsilon = 0.01$ the temperature solutions are aligned with the temperature model 1 PV in the outer part where the profiles are adiabatic. For the rest of the profile, all temperature solutions are higher than the temperature model 1 PV. For $\epsilon = 0.001$, there were only temperature solutions found that are always higher than the temperature model 1 PV.

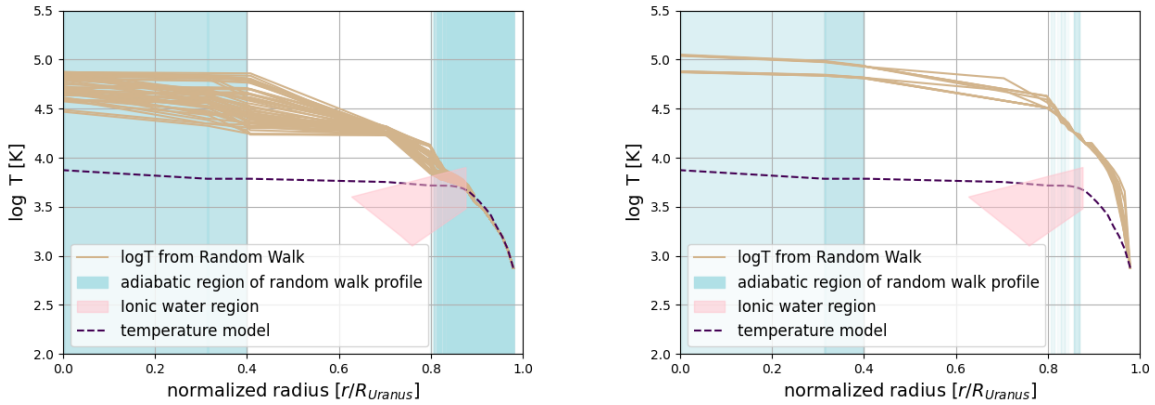

(a) with $\beta = 1$ and $\epsilon = 0.01$ (b) with $\beta = 1$ and $\epsilon = 0.001$

Figure 14: Temperature solutions for density and temperature model 1 PV from [15]

Figure 15 shows the temperature solutions for the density and the temperature model 2 PV from [15]. In figure 15a $\beta = 0.5$ was used for the temperature gradient limit while in figure 15b $\beta = 1$ was used. Both cases use $\epsilon = 0.01$. In the outer part, there is a region where all temperature

solutions are aligned with the 2 PV temperature model. This region is also adiabatic. For β = 0.5 except for one single profile, all temperature solutions are slightly lower than the 2 PV temperature model. For β = 1 except for the outer part all temperature solutions are higher than the 2 PV temperature model. For ϵ = 0.001 no temperature solutions were found.

Figures 15c and 15d show the associated entropy as a function of the normalized radius for the temperature profiles in figures 15a and 15b. The entropy plots show that in a region where at least one of the entropy solutions remains sufficiently constant the region gets labeled as adiabatic.

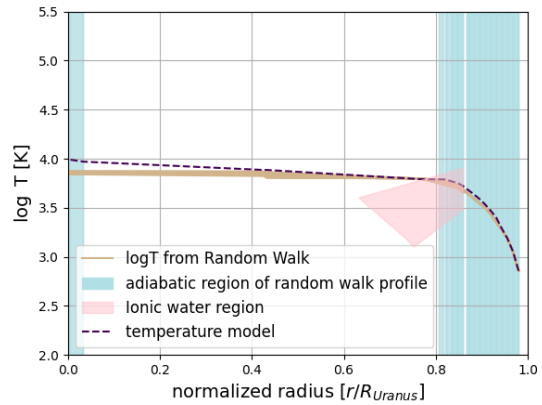

(a) with β = 0.5 and ϵ = 0.01

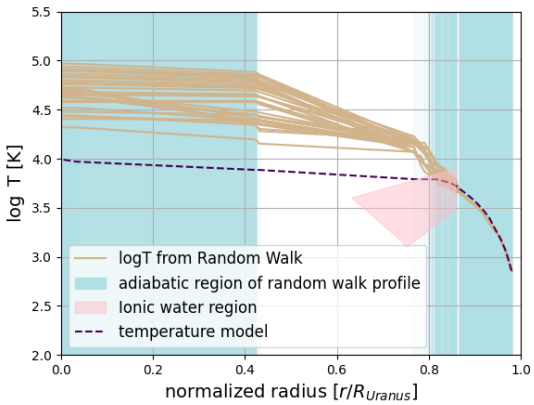

(b) with β = 1 and ϵ = 0.01

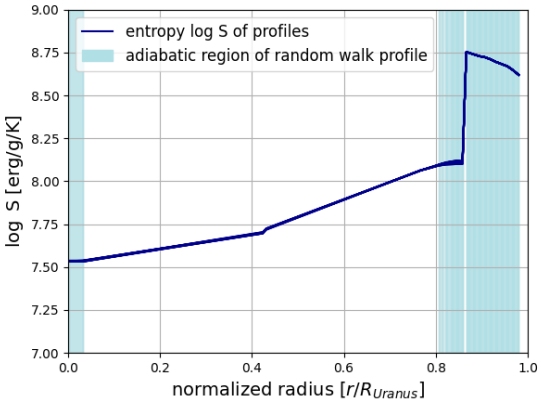

(c) with β = 0.5 and ϵ = 0.01

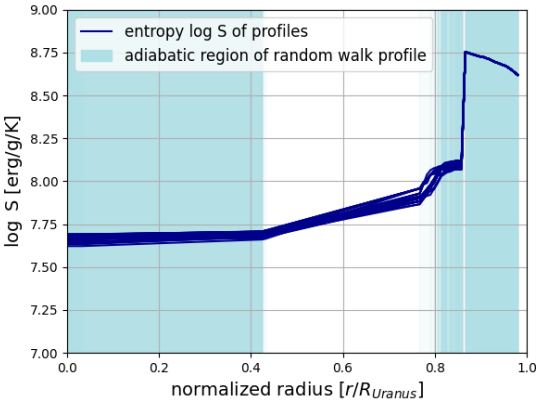

(d) with β = 1 and ϵ = 0.01

Figure 15: Temperature solutions for density and temperature model 2 PV from [15]

Figure 16 shows the temperature solutions for the density and the temperature model 3 PV from [15]. In figure 16a ϵ = 0.01 was used for the entropy constraint while in figure 16b ϵ = 0.001 was used. Both cases use β = 1. For the smaller β values 0.5 and 0.1 no solutions were found. For ϵ = 0.01 the temperature solutions are aligned with the temperature model 3 PV in the outer part where the profiles are adiabatic. For the rest of the profiles region, all temperature solutions are higher than the temperature model 3 PV. For ϵ = 0.001, there was only one temperature solution found which is always higher than the temperature model 3 PV.

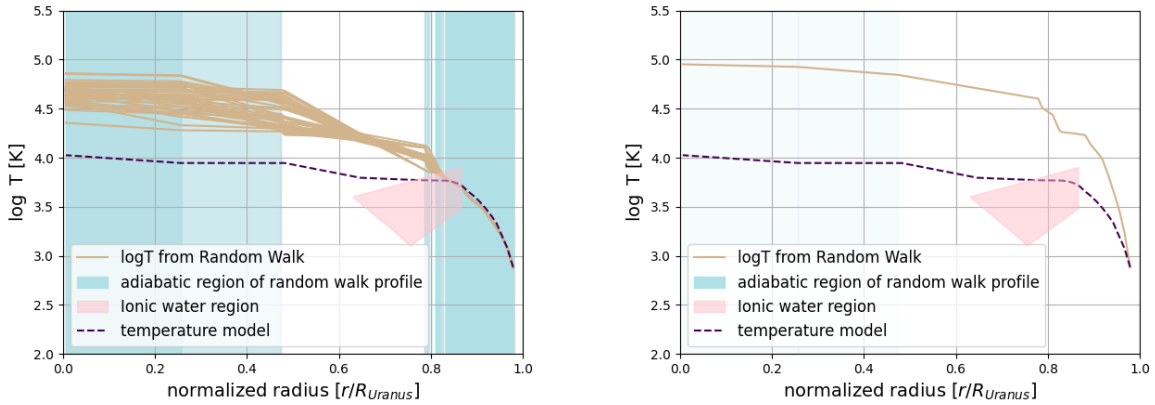

(a) with $\beta = 1$ and $\epsilon = 0.01$

(b) with $\beta = 1$ and $\epsilon = 0.001$

Figure 16: Temperature solutions for density and temperature model 3 PV from [15]

Figure 17 shows the temperature solutions for the density and the temperature model 4 PV from [15]. In figures 17a,17a and 17c the values of β are set to 0.1, 0.5 and 1. All of them use $\epsilon = 0.01$ for the entropy constraint. In figure 17d $\beta = 1$ and $\epsilon = 0.001$ were used. For $\epsilon = 0.01$ the temperature solutions are aligned with the temperature model 4 PV in the outer part where the profiles are adiabatic. For $\beta = 0.1$, the temperature solutions are also close to the temperature model 4 PV for the inner part. For $\beta = 0.5$ the temperature solutions cover the region of the temperature model in the middle part and are higher in the center. For $\beta = 1$, the temperature solutions are higher than the temperature model for the majority of the profile. For $\epsilon = 0.001$, the temperature solutions are always higher than the temperature model 4 PV even in the outer region.

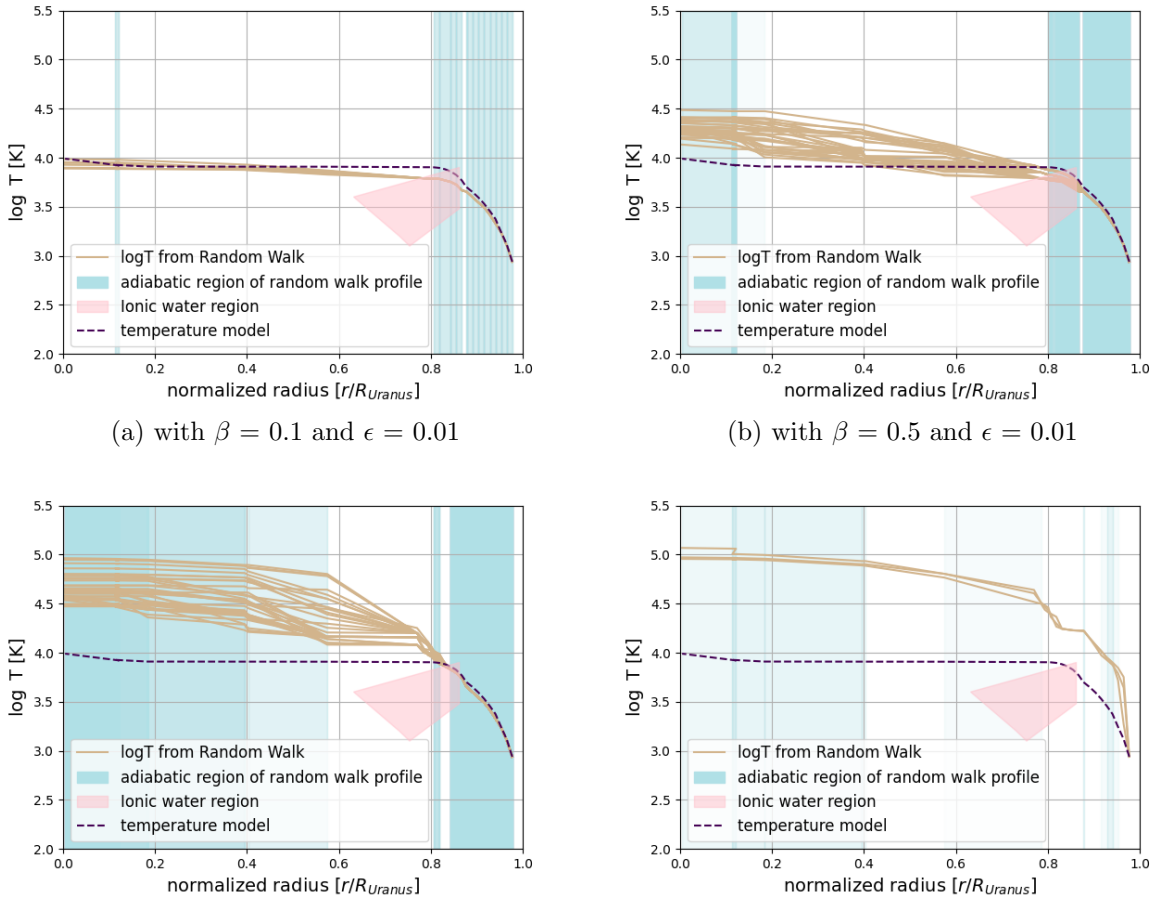

(a) with $\beta = 0.1$ and $\epsilon = 0.01$

(b) with $\beta = 0.5$ and $\epsilon = 0.01$

(c) with $\beta = 1$ and $\epsilon = 0.01$

(d) with $\beta = 1$ and $\epsilon = 0.001$

Figure 17: Temperature solutions for density and temperature model 4 PV from [15]

Figure 18 shows the temperature solutions for the density and the temperature model 5 PV from [15] In figure 18a $\epsilon = 0.01$ was used for the entropy constraint while in figure 18b $\epsilon = 0.001$ was used. Both cases use $\beta = 1$. For the smaller β values 0.5 and 0.1 no solutions were found. For $\epsilon = 0.01$ the temperature solutions are aligned with the temperature model 5 PV in the outer part where the profiles are adiabatic. For the rest of the profile, all temperature solutions are higher than the temperature model 5 PV. For $\epsilon = 0.001$, the temperature solutions are always higher than the temperature model 4 PV.

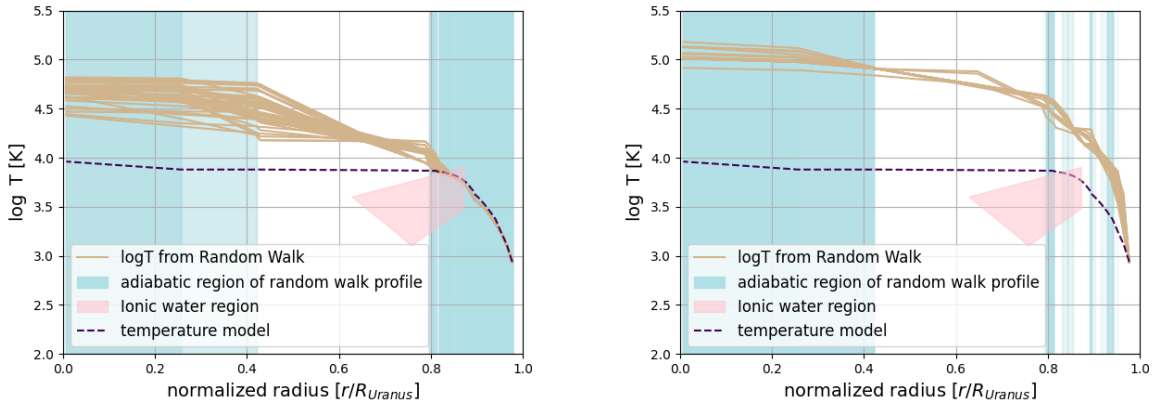

(a) with $\beta = 1$ and $\epsilon = 0.01$ (b) with $\beta = 1$ and $\epsilon = 0.001$

Figure 18: Temperature solutions for density and temperature model 5 PV from [15]

The figures in this section show that the choice of β and ϵ can have a great impact on the number of solutions found and the compatibility of the temperature solutions and the temperature models. In contrast to section 4.1.1 in this section the choice of $\epsilon = 0.001$ never provides compatible solutions. In most cases there are only very few solutions found with this ϵ value and the solutions are always much higher than the temperature model. With $\epsilon = 0.01$ all models are compatible with the temperature solutions at least for a part in the outer adiabatic region. The range of this compatible region varies for the different models but doesn't depend much on β. For some models namely 1 PV, 3 PV and 5 PV the temperature models are always lower than the temperature solutions except for the outer region. Compatible solutions can't be found for those models since for lower β values, that could provide lower temperature solutions, no solutions are found. For the models 1 CC and 1 PH it is possible to find solutions matching the central temperatures of the models. However, for the solutions with matching central temperatures there is always a region towards the outer part where the temperature solutions aren't well aligned with the temperature model. The models 2 PV and 4 PV have the best compatibility with the temperature solutions. For both cases, it is possible to find temperature solutions that are close to the temperature models at any radius. With a more suitable choice of β for those models, it might be possible to find solutions even closer to the temperature models. For all profiles in this section a choice of $\beta = 1$ leads to central temperature solutions that are always higher than the ones of the reference models. Matching central temperatures can only be found for smaller β values, which agrees well with our expectations of β being smaller than 1 as presented in section 3.2.3.

4.2 Composition and temperature models

In this part, the random walk algorithm will be used on the density models shown in figure 4b. For those density models solutions of temperature and composition can be found for the whole range of the planet, starting at the surface at a pressure of 1 bar until the center of Uranus. The start temperature at the surface used for the calculations of the models in this section is 100 K. The composition starts with a combination of hydrogen-helium and water. In this section, the entropy constraint, as articulated in equation 18, is applied with ϵ= 0.01. With smaller ϵ values such as $\epsilon = 0.001$, only a limited number of solutions were found, making smaller values unsuitable for the analysis. The random walk algorithm was implemented for different β values for the temperature gradient limits in equation 19. Results for β values of 1, 0.5, and 0.1 are presented in sections 4.2.1, 4.2.2, and 4.2.3, respectively. In this section, the temperature and composition solutions for a selection of density profiles are shown. The selection of density profiles should reflect temperature and composition solutions that are as different as possible to give an impression of the solution range. The plots in this section show the temperature and composition solutions found by the random walk algorithm as well as the ionic water region shown as a pink area. The blue background on the plots indicates the regions where at least one of the temperature solutions has an adiabatic gradient (following the condition from section 3.2.2). The composition results in this section have a strong connection to the central temperature results. Therefore to interpret the compositions in terms of total mass fraction the profiles are divided into four different categories by means of their central temperature: the "reference temperature models", the "moderate models", the "hot models" and the "extreme hot models". The "reference temperature models" are defined as models with central temperatures in the range $\log T_c$ = (3.3 - 4.5) K as the published models shown in figure 5 which corresponds to $T_c \approx$ (2000 - 31 600) K. The "moderate models" are defined as models with central temperatures in the range $\log T_c$ = (4.5 - 4.9) K which corresponds to $T_c \approx$ (31 600 - 79 400) K. The "hot models" are defined as models with central temperatures in the range $\log T_c$ = (4.9 - 5.05) K which corresponds to $T_c \approx$ (79 400 - 112 200) K. The "extreme hot models" are defined as models with central temperatures higher than $\log T_c = 5.05$ K which corresponds to $T_c \approx$ 112 200 K.

4.2.1 Models with $\beta = 1$

The models shown in this section were calculated with $\beta = 1$ for the Ledoux criterion (equation 19). Figure 19 shows the temperature solutions found for the density models from figure 4b as a function of the normalized mass. The color on the plots indicates the profile number. Models with higher profile numbers have higher central densities. Central temperatures for profiles with higher central densities are within a narrower range, situated towards the lower end of the overall range of central temperatures. For lower central densities the according central temperatures cover a broader range. In figure 19a all temperature solutions found are shown while in figure 19b only the temperature profiles with adiabatic solutions in the ionic water region are shown.

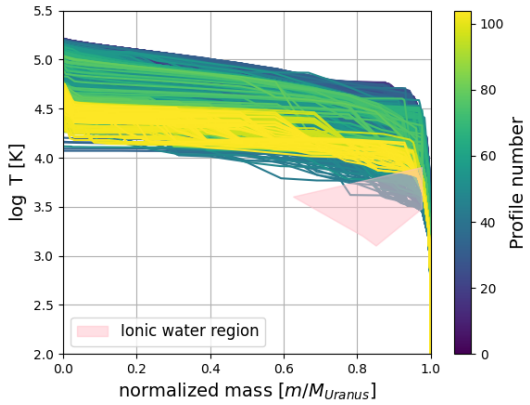

(a) All temperature profiles found for density models in figure 4b

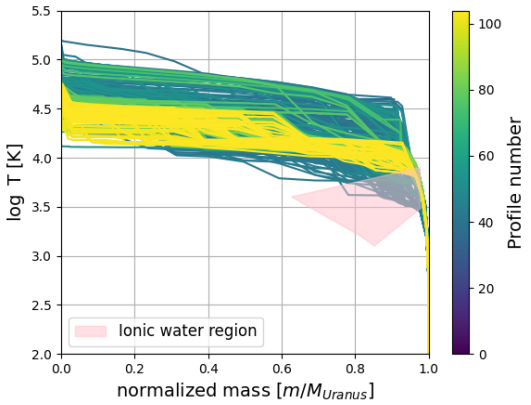

(b) Only temperature profiles with adiabatic solutions in the ionic water region

Figure 19: Temperature solutions as a function of the normalized mass with $\beta = 1$ for all density models from figure 4b

Figure 20 shows the distribution of the central temperatures and points out the range of central temperatures found. Since $\beta = 1$ allows the highest temperature gradient, the central temperatures found can reach very high values. The majority of the central temperatures are higher than the range of central temperature from previous models shown in figure 5.

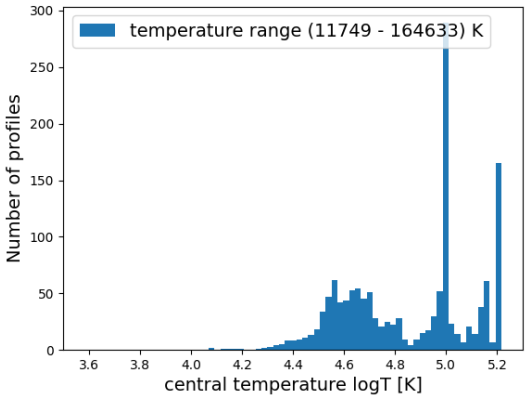

(a) All temperature profiles found for density models in figure 4b

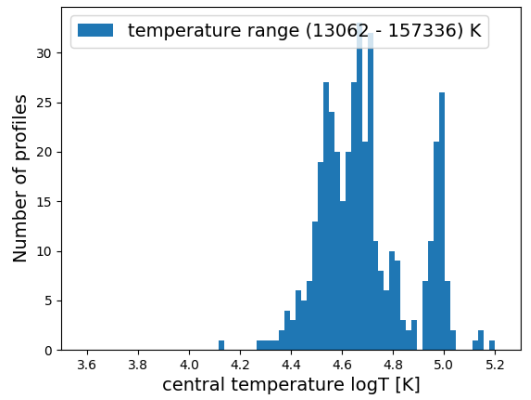

(b) Only temperature profiles with adiabatic solutions in the ionic water region

Figure 20: Histograms of the central temperatures with $\beta = 1$

For all temperature solutions in figure 20a we get a central temperature range of $\log T_c$ = (4.07 - 5.22) K which corresponds to T_c = (1.1 - 16.5) $\cdot 10^4$ K. If we only consider the profiles with adiabatic solutions in the ionic water range as shown in figure 20b we get a more narrow central temperature range. If outliers are neglected we get a central temperature range of $\log T_c$ = (4.25 - 5.05) K which corresponds to T_c = (1.7 - 11.3) $\cdot 10^4$ K. In both scenarios, the majority of central temperatures exceed the range represented by the temperature models in previous research, where the central temperatures were within the range $\log T_c$ = (3.3 - 4.5) K, as illustrated in figure 5.

Figure 21 shows the composition and temperature results for the density model 102. In figure 21a and 21b the composition and temperature results are plotted against the normalized mass while in figure 21c and 21d the results are plotted against the normalized radius. The example shows that the inner and outer parts are more visible if the results are shown as a function of the radius. However, when the results are plotted against mass, it provides a more accurate representation of the composition in terms of mass. The temperature plots show that the solutions found for this density profile have adiabatic temperature gradients in the ionic water region and a composition that contains water in the same region. This combination could allow the creation of a dynamo for the magnetic field.

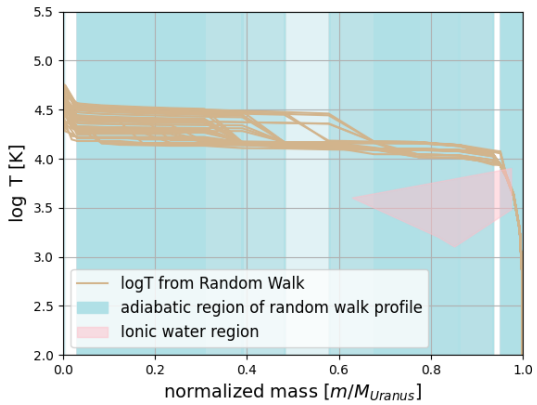

(a) Temperature solutions as a function of the normalized mass

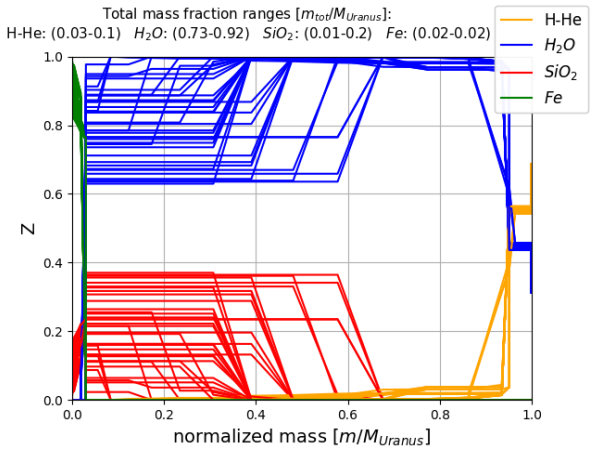

(b) Mass fraction solutions as a function of the normalized mass

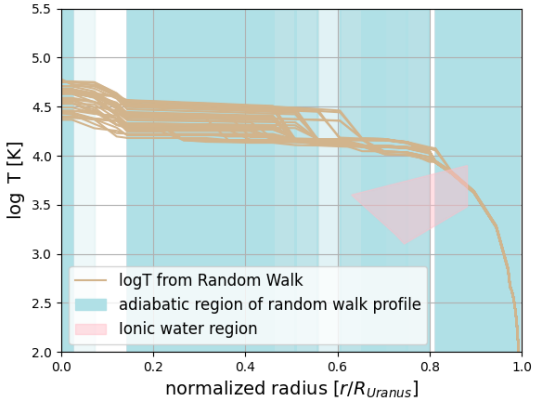

(c) Temperature solutions as a function of the normalized radius

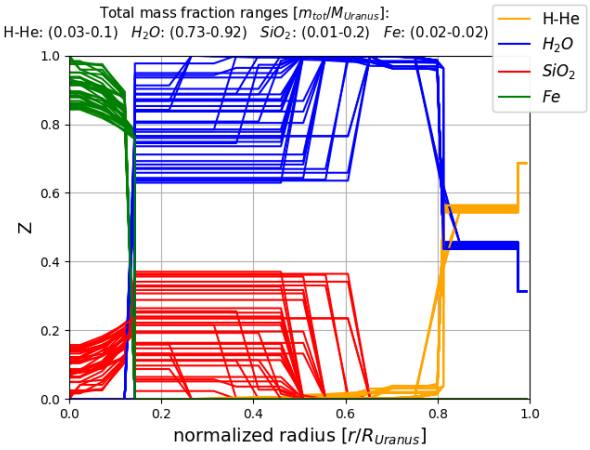

(d) Mass fraction solutions as a function of the normalized radius

Figure 21: Composition and temperature results for the density model 102 with $\beta = 1$ and $\epsilon = 0.01$

Figure 22 shows the composition and temperature results for the density model 24 as a function of the normalized mass. All central temperatures found are very high. One single solution with a central temperature higher than $\log T_c = 5$ suggesting a high iron mass fraction may be considered an outlier and can likely be disregarded. For this density profile, no solution is found to be adiabatic and in the ionic water region at the same time.

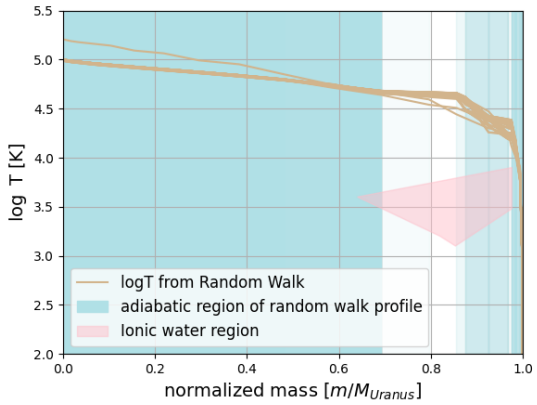

(a) Temperature solutions as a function of the normalized mass

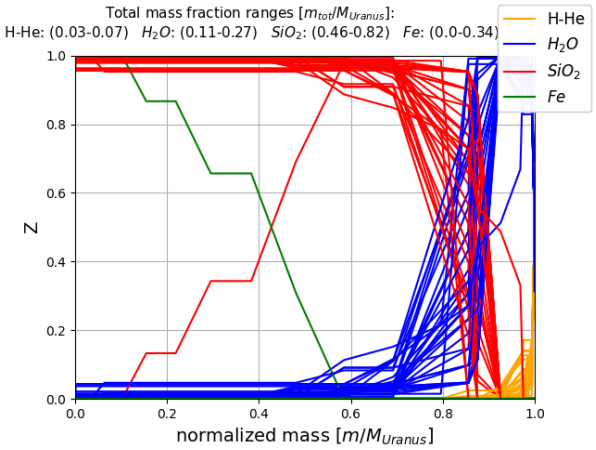

(b) Mass fraction solutions as a function of the normalized mass

Figure 22: Composition and temperature results for the density model 24 with $\beta = 1$ and $\epsilon = 0.01$

Figure 23 shows the composition and temperature results for the density model 43 as a function of the normalized mass. The temperature plots show that the solutions found for this density profile have adiabatic temperature gradients in the ionic water region and a composition that contains water in the same region.

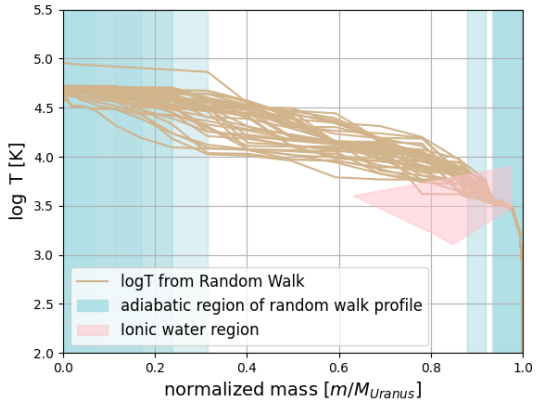

(a) Temperature solutions as a function of the normalized mass

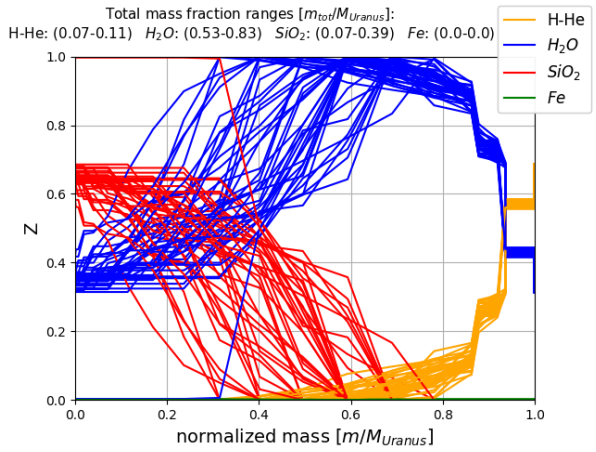

(b) Mass fraction solutions as a function of the normalized mass

Figure 23: Composition and temperature results for the density model 43 with $\beta = 1$ and $\epsilon = 0.01$

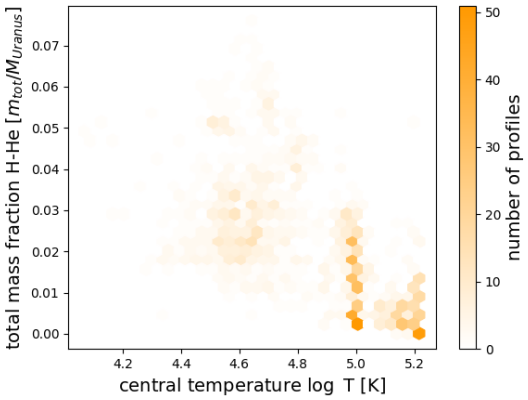

(a) Total mass fraction of $H - He$ as a function of the central temperature

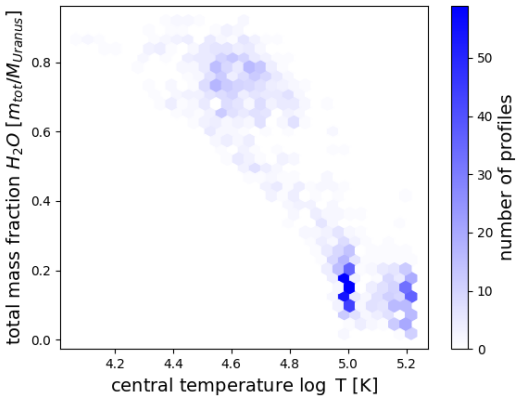

(b) Total mass fraction of H_2O as a function of the central temperature

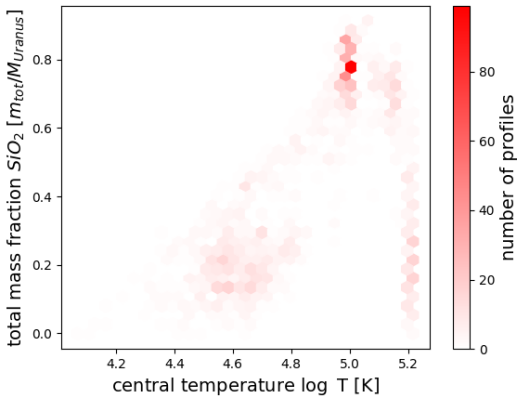

(c) Total mass fraction of SiO_2 as a function of the central temperature

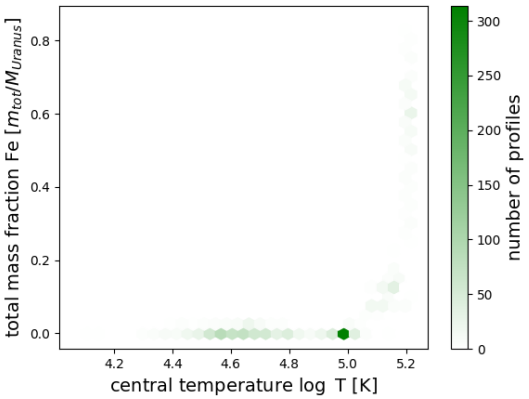

(d) Total mass fraction of Fe as a function of the central temperature

Figure 24: Total mass fractions as a function of the central temperature for $\beta = 1$

Figure 24 shows the total mass fractions of all components as a function of the profile's central temperatures. The total $H - He$ mass fraction is lower than 0.07 for all profiles in this section. The total mass fraction of H_2O and SiO_2 can be at almost any value and depends on the central temperature. The total mass fraction of Fe is very low for most of the profiles and reaches higher values only for very hot central temperatures. In table 3 the total ranges of total mass fraction for all components are shown split up into the four different temperature model categories: "reference temperature model", "moderate model", "hot model", "extreme hot model". Outliers are neglected in the determination of the total mass fraction range.

	reference temperature models	moderate models	hot models	extreme hot models
$\log T_c$ [K]	3.3 - 4.5	4.5 - 4.9	4.9 - 5.05	> 5.05
number of models	82	586	434	317
$H-He$	0.01 - 0.06	0.01 - 0.06	0.00 - 0.04	0.00 - 0.03
H_2O	0.62 - 0.92	0.28 - 0.92	0.02 - 0.40	0.01 - 0.25
SiO_2	0.00 - 0.30	0.00 - 0.67	0.26 - 0.92	0.01 - 0.92
Fe	0.00 - 0.03	0.00 - 0.03	0.00 - 0.36	0.00 - 0.86

Table 3: Total mass fractions for all components in different model categories for $\beta = 1$

4.2.2 Models with $\beta = 0.5$

The models shown in this section were calculated with $\beta = 0.5$ for the Ledoux criterion (equation 19). Figure 25 shows the temperature solutions found for all density models from figure 4b as a function of the normalized mass. The color on the plots indicates the profile number. Models with higher profile numbers have higher central densities. Central temperatures for profiles with higher central densities are within a narrower range, situated towards the lower end of the overall range of central temperatures. For lower central densities the according central temperatures cover a broader range. In figure 25a all temperature solutions found are shown while in figure 25b only the temperature profiles with adiabatic solutions in the ionic water region are shown.

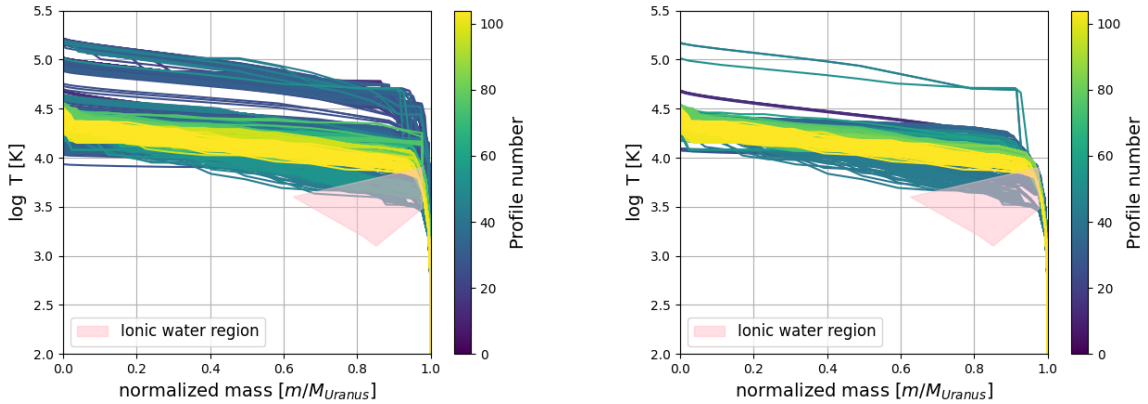

(a) All temperature profiles found for density models in figure 4b

(b) Only temperature profiles with adiabatic solutions in the ionic water region

Figure 25: Temperature solutions as a function of the normalized mass with $\beta = 0.5$ for all density models from figure 4b

Figure 26 shows the distribution of the central temperatures and points out the range of central temperatures found. The temperature gradient is limited to a lower gradient with $\beta = 0.5$. The central temperatures have a more pronounced concentration around a main peak compared to the case of $\beta = 1$. The main peak at $\log T_c = 4.4$ K and two smaller peaks at higher temperatures are still higher than most of the central temperatures from previous models.

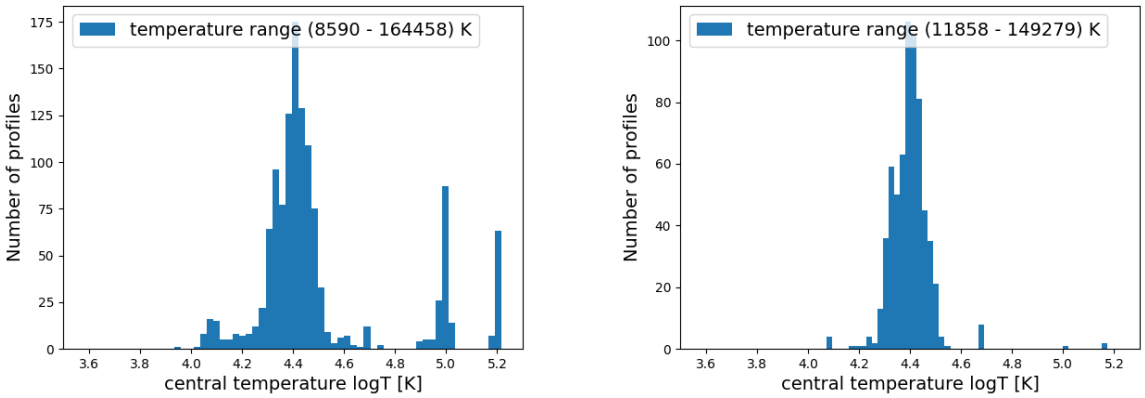

(a) All temperature profiles found for density models in figure 4b

(b) Only temperature profiles with adiabatic solutions in the ionic water region

Figure 26: Histogram of the central temperatures with $\beta = 0.5$

For all temperature solutions in figure 26a we get a central temperature range of $\log T_c$ = (3.9 - 5.22) K which corresponds to T_c = (0.8 - 16.5) $\cdot 10^4$ K. If we only consider the profiles with adiabatic solutions in the ionic water range as shown in figure 26b we get a more narrow central temperature range. If outliers are neglected we get a central temperature range of $\log T_c$ = (4.15 - 4.56) K which corresponds to T_c = (1.4 - 3.7) $\cdot 10^4$ K. Considering all temperature solutions many solutions exceed the range represented by the temperature models in previous research. Considering only the profiles with adiabatic solutions in the ionic water range almost all central temperatures lie within the range $\log T_c$ = (3.3 - 4.5) K, as illustrated in figure 5.

Figure 27 shows the composition and temperature results for the density model 79. In figure 27a and 27b the composition and temperature results are plotted against the normalized mass while in figure 27c and 27d the results are plotted against the normalized radius to enhance the visibility of the composition in both the central and outer regions. The temperature plots show that the solutions found for this density profile have adiabatic temperature gradients in the ionic water region and a composition that contains water in the same region.

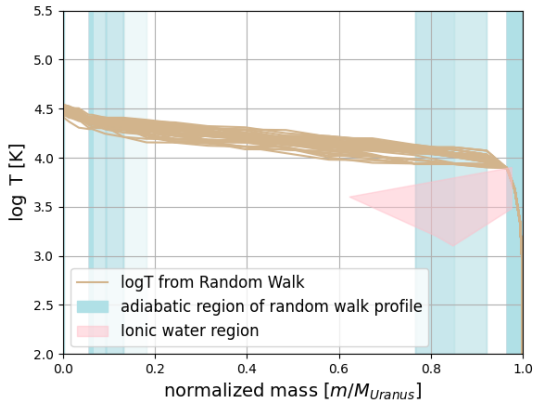

(a) Temperature solutions as a function of the normalized mass

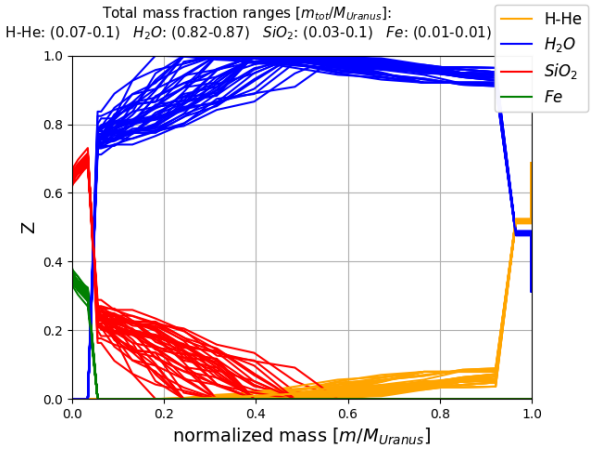

(b) Mass fraction solutions as a function of the normalized mass

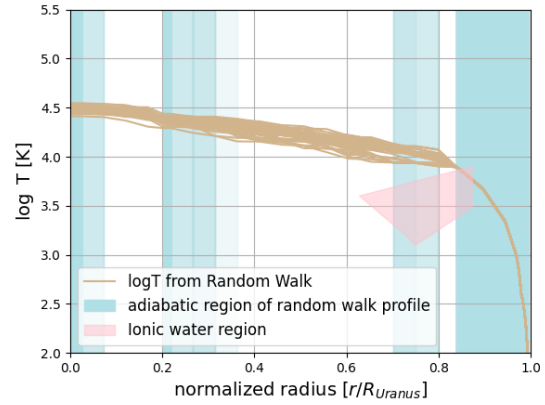

(c) Temperature solutions as a function of the normalized radius

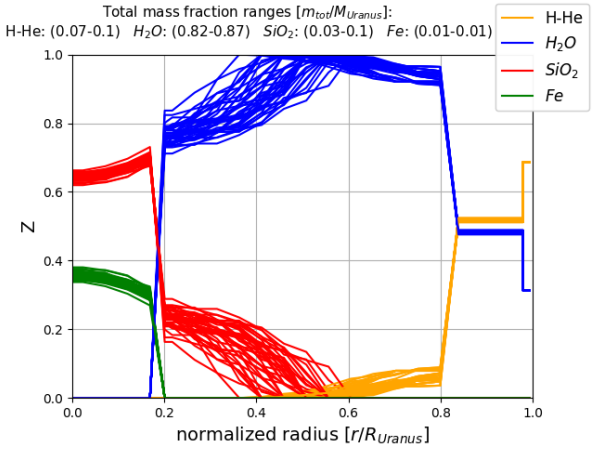

(d) Mass fraction solutions as a function of the normalized radius

Figure 27: Composition and temperature results for the density model 79 with $\beta = 0.5$ and $\epsilon = 0.01$

Figure 28 shows the composition and temperature results for the density model 13. The temperature plot shows that the profiles found are adiabatic over the whole range of the planet and are therefore all almost identical since for an adiabatic profile the temperature gradient is unique and therefore gives only one option for the solution. In the ionic water region, the composition also contains water, and since the whole profile is adiabatic it also has an adiabatic temperature gradient in that region. Since that whole profile range is adiabatic the composition remains constant except for one jump.

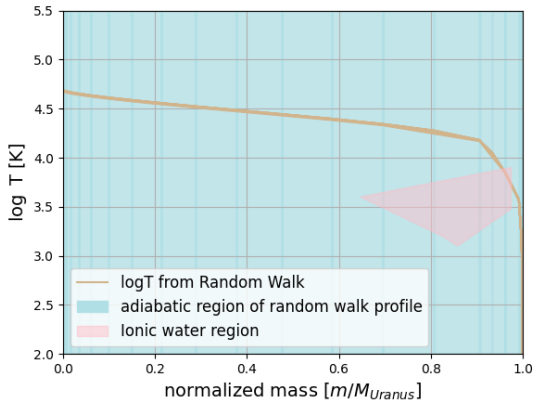

(a) Temperature solutions as a function of the normalized mass

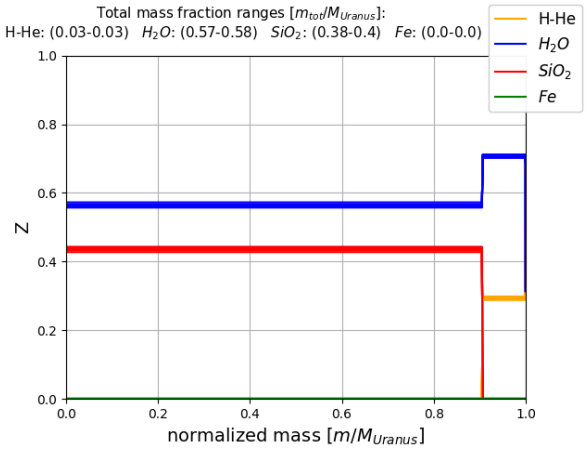

(b) Mass fraction solutions as a function of the normalized mass

Figure 28: Composition and temperature results for the density model 13 with $\beta = 0.5$ and $\epsilon = 0.01$

Figure 29 shows the composition and temperature results for the density model 63. The temperature plot shows that a major part of the profile is adiabatic and therefore the profiles are very similar. For this density profile, no solution is found to be adiabatic and in the ionic water region at the same time.

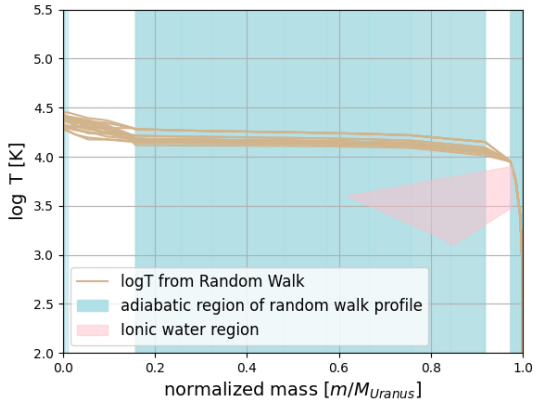

(a) Temperature solutions as a function of the normalized mass

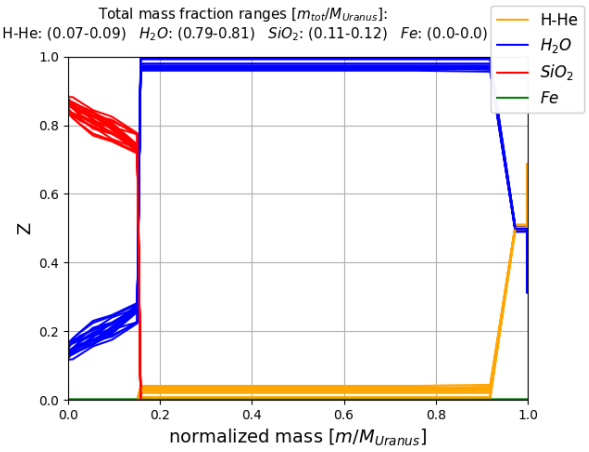

(b) Mass fraction solutions as a function of the normalized mass

Figure 29: Composition and temperature results for the density model 63 with $\beta = 0.5$ and $\epsilon = 0.01$

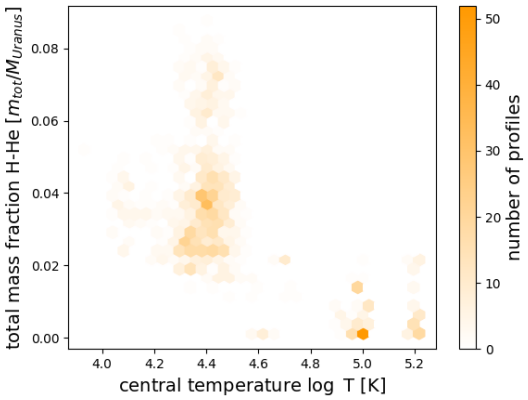

(a) Total mass fraction of $H - He$ as a function of the central temperature

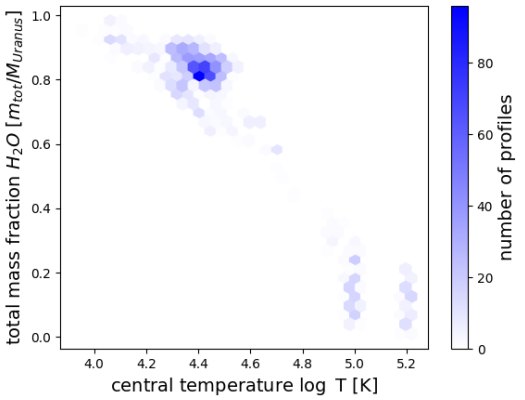

(b) Total mass fraction of H_2O as a function of the central temperature

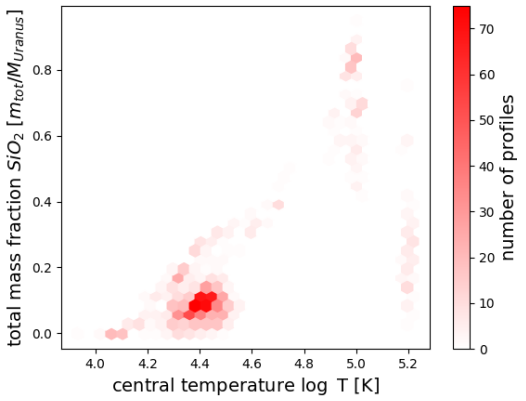

(c) Total mass fraction of SiO_2 as a function of the central temperature

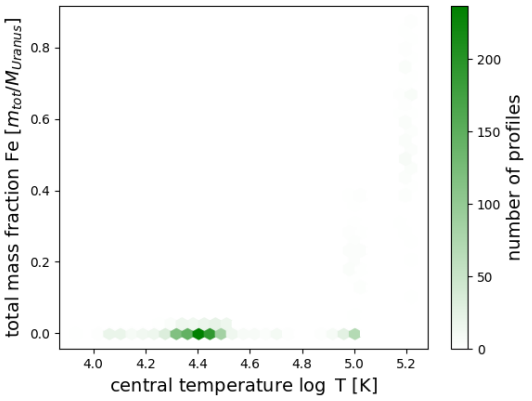

(d) Total mass fraction of Fe as a function of the central temperature

Figure 30: Total mass fractions as a function of the central temperature for $\beta = 0.5$

Figure 30 shows the total mass fractions of all components as a function of the profile's central temperatures. The total $H - He$ mass fraction is lower than 0.08 for all profiles in this section. The total mass fraction of H_2O and SiO_2 can be at almost any value and depends on the central temperature. The total mass fraction of Fe is very low for most of the profiles and reaches higher values only for very hot central temperatures. In table 4 the total ranges of total mass fraction for all components are shown split up into the four different temperature model categories: "reference temperature model", "moderate model", "hot model", "extreme hot model". Outliers are neglected in the determination of the total mass fraction range.

	reference temperature models	moderate models	hot models	extreme hot models
$\log T_c$ [K]	3.3 - 4.5	4.5 - 4.9	4.9 - 5.05	> 5.05
number of models	964	73	138	70
$H-He$	0.01 - 0.08	0.00 - 0.07	0.00 - 0.02	0.00 - 0.03
H_2O	0.64 - 0.98	0.55 - 0.87	0.03 - 0.37	0.01 - 0.23
SiO_2	0.00 - 0.31	0.01 - 0.42	0.43 - 0.95	0.03 - 0.76
Fe	0.00 - 0.02	0.00 - 0.02	0.00 - 0.39	0.09 - 0.88

Table 4: Total mass fractions for all components in different model categories for $\beta = 0.5$

4.2.3 Models with $\beta = 0.1$

The models shown in this section were calculated with $\beta = 0.1$ for the Ledoux criterion (equation 19). Figure 31 shows the temperature solutions found for all density models from figure 4b as a function of the normalized mass. The color on the plots indicates the profile number. Models with higher profile numbers have higher central densities. Central temperatures for profiles with higher central densities are within a narrower range, situated towards the lower end of the overall range of central temperatures. For lower central densities the according central temperatures cover a broader range. In figure 31a all temperature solutions found are shown while in figure 31b only the temperature profiles with adiabatic solutions in the ionic water region are shown.

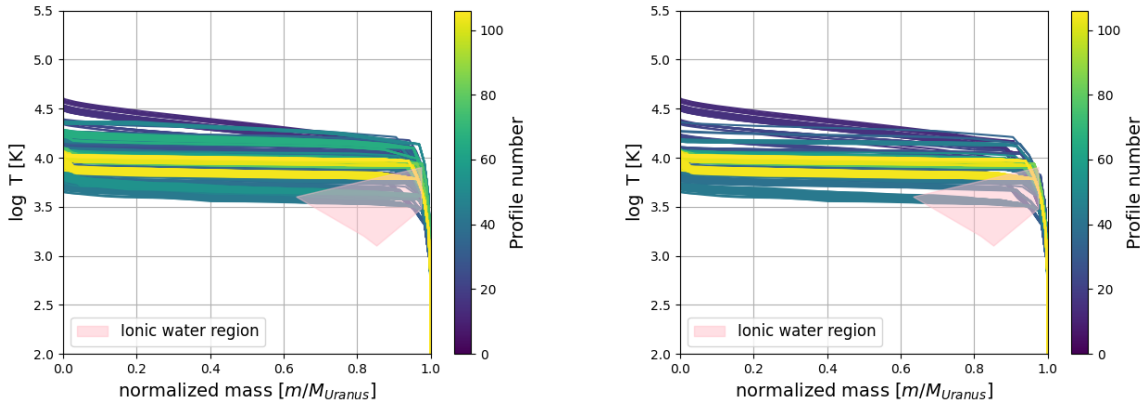

(a) All temperature profiles found for density models in figure 4b

(b) Only temperature profiles with adiabatic solutions in the ionic water region

Figure 31: Temperature solutions as a function of the normalized mass with $\beta = 0.1$ for all density models from figure 4b

Figure 32 shows the distribution of the central temperatures and points out the range of central temperatures found. The temperature gradient is limited to a lower gradient with $\beta = 0.1$. The central temperatures are concentrated around a main peak at a lower temperature compared to the case of $\beta = 1$ and $\beta = 0.5$. Most of the central temperatures in this case are in the same range as the temperatures from previous models.

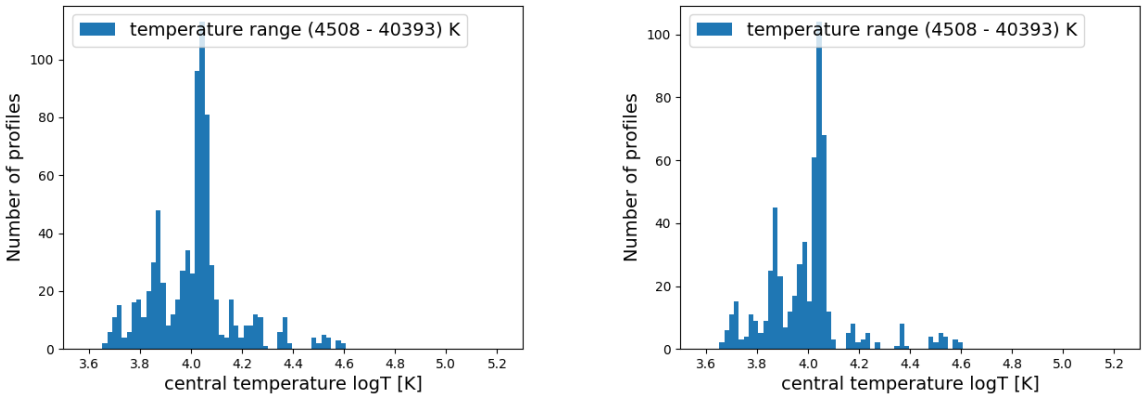

(a) All temperature profiles found for density models in figure 4b

(b) Only temperature profiles with adiabatic solutions in the ionic water region

Figure 32: Histogram of the central temperatures with $\beta = 0.1$

For all temperature solutions in figure 32a we get a central temperature range of $\log T_c =$ (3.63 - 4.6) K which corresponds to $T_c = (0.45 - 4.04) \cdot 10^4$ K. Considering only the profiles with adiabatic solutions in the ionic water range as shown in figure 26b leads only to a very small change in the central temperature distribution and has no impact on the central temperature range. A great majority of the temperature solutions have central temperatures that lie within the range represented by the temperature models in previous research, where the central temperatures were within the range $\log T_c =$ (3.3 - 4.5) K, as illustrated in figure 5.

Figure 33 shows the composition and temperature results for the density model 84. In figure 33a and 33b the composition and temperature results are plotted against the normalized mass while in figure 33c and 33d the results are plotted against the normalized radius. The temperature plots show that the solutions found for this density profile have adiabatic temperature gradients in the ionic water region and a composition that contains water in the same region. The solutions are all very similar.

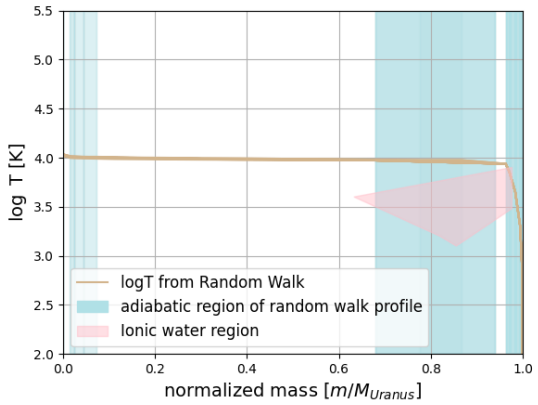

(a) Temperature solutions as a function of the normalized mass

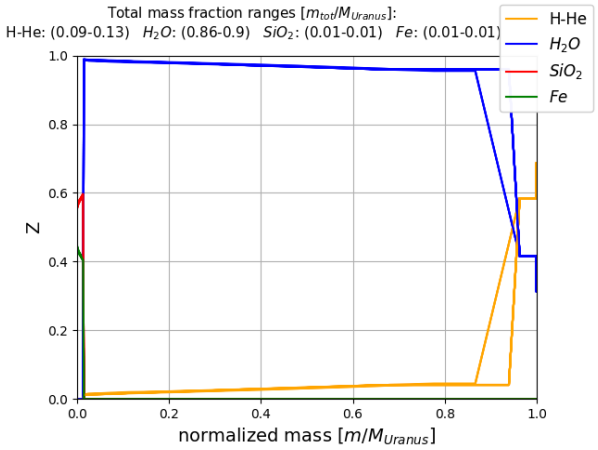

(b) Mass fraction solutions as a function of the normalized mass

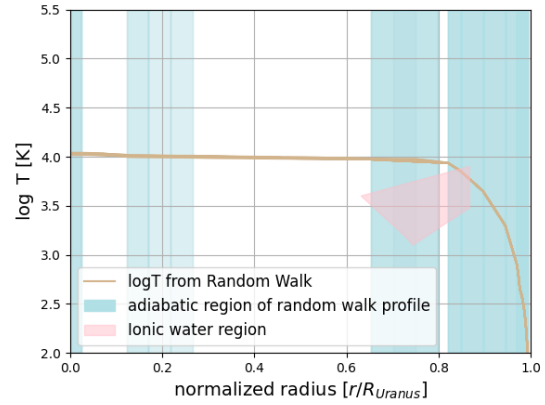

(c) Temperature solutions as a function of the normalized radius

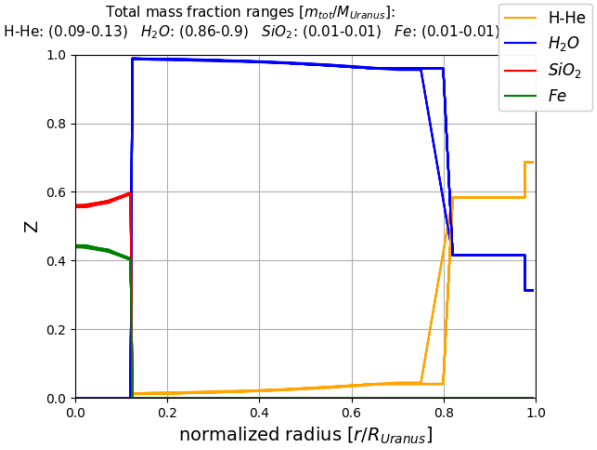

(d) Mass fraction solutions as a function of the normalized radius

Figure 33: Composition and temperature results for the density model 84 with $\beta = 0.1$ and $\epsilon = 0.01$

Figure 34 shows the composition and temperature results for the density model 54 as a function of the normalized mass. There is an adiabatic temperature region with water in the composition that has an overlap with the ionic water region, however, the overlap is very small.

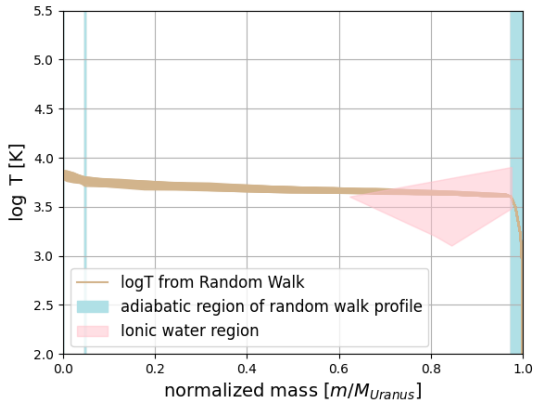

(a) Temperature solutions as a function of the normalized mass

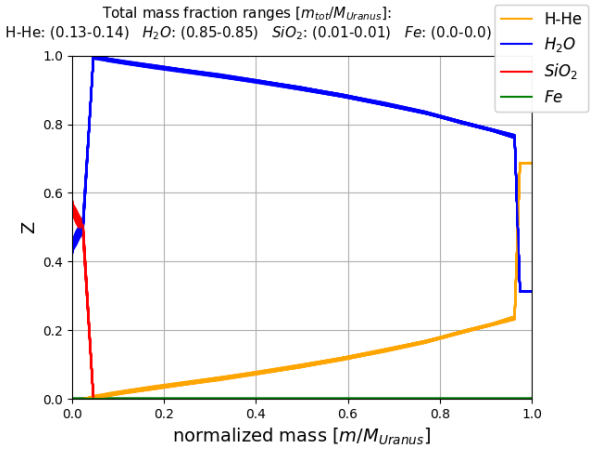

(b) Mass fraction solutions as a function of the normalized mass

Figure 34: Composition and temperature results for the density model 54 with $\beta = 0.1$ and $\epsilon = 0.01$

Figure 35 shows the composition and temperature results for the density model 33 as a function of the normalized mass. The temperature plots show that the solutions found for this density profile have adiabatic temperature gradients in the ionic water region and a composition that contains water in the same region. The composition for this profile only contains water, hydrogen and helium while most of the profiles contain also SiO_2 at least towards the center.

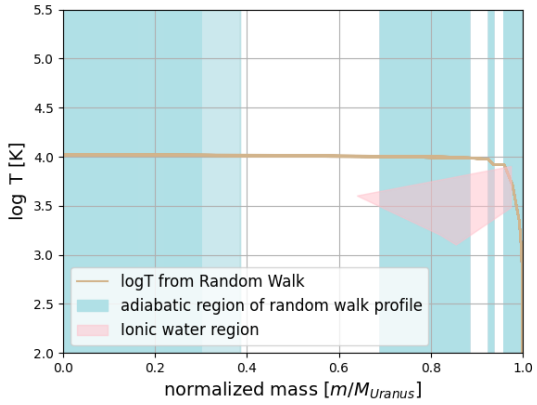

(a) Temperature solutions as a function of the normalized mass

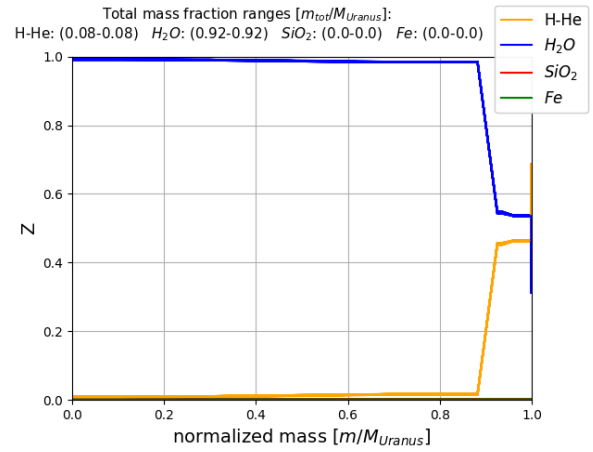

(b) Mass fraction solutions as a function of the normalized mass

Figure 35: Composition and temperature results for the density model 33 with $\beta = 0.1$ and $\epsilon = 0.01$

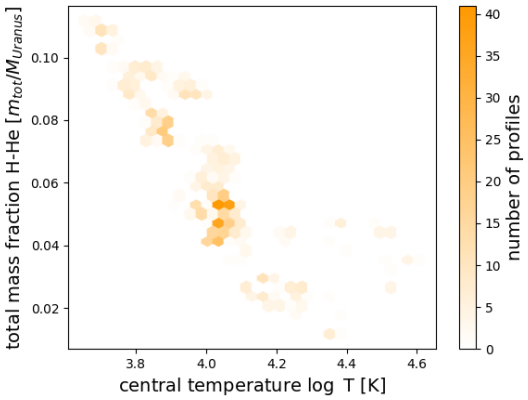

(a) Total mass fraction of $H - He$ as a function of the central temperature

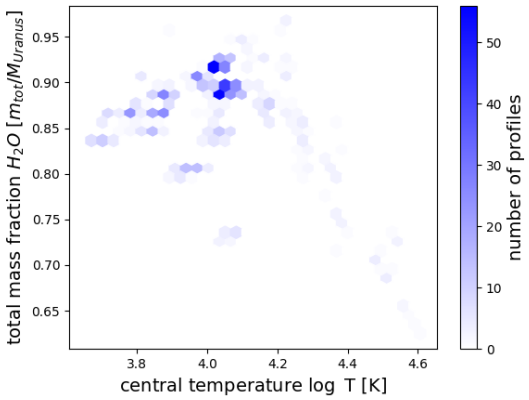

(b) Total mass fraction of H_2O as a function of the central temperature

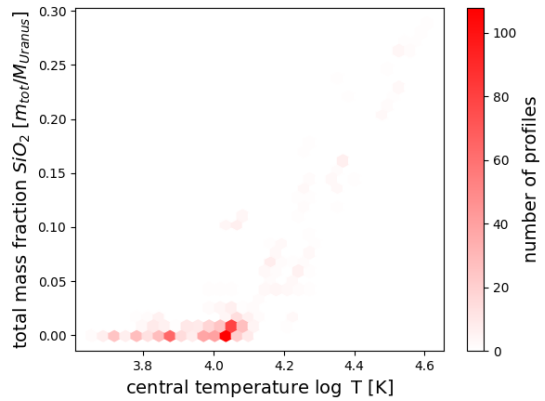

(c) Total mass fraction of SiO_2 as a function of the central temperature

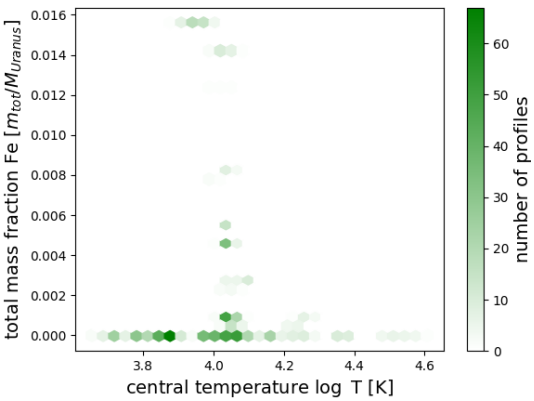

(d) Total mass fraction of Fe as a function of the central temperature

Figure 36: Total mass fractions as a function of the central temperature for $\beta = 0.1$

Figure 36 shows the total mass fractions of all components as a function of the profiles central temperatures. Since central temperature higher than $\log T_c = 4.5$ are very rare in this section we are only discussing the total mass fraction ranges for the "reference temperature models". The total $H - He$ mass fraction range is between 0.01 and 0.12. The total mass fraction of H_2O is in a range between 0.7 and 0.96. For SiO_2 the total mass fractions are all below 0.3, and most of them are in a range between 0 and 0.04. The total mass fraction of Fe is between 0 and 0.016.

4.3 Discussion of total bulk compositions and different β values

In this thesis, the random walk algorithm was implemented for the values $\beta = 1$, 0.5, 0.1. In section 4.1 temperature solutions were derived for those β values and compared to reference temperature models. In section 4.2 temperature and composition solutions were derived for each of those β values.

As already stated in section 3.2.3 β is probably smaller than one maybe even significantly smaller. However, it is difficult to say more precisely what value we should expect for β. In section 4.1 we can see that for $\beta = 1$, the solutions if they even exist have always higher central temperatures than the reference models. If we trust the reference models this supports the assumption that β should probably be smaller than 1. For $\beta = 0.1$ and $\beta = 0.5$ many central temperature solutions were found in the range of the reference models. The temperature results from section 4.2 also show that for $\beta = 1$ many central temperatures higher than 10^5 K are found and for almost all solutions the central temperatures are higher than the central temperature range of the reference models which is between $10^{3.3}$ K and $10^{4.5}$ K. For $\beta = 0.5$ some central temperature higher than 10^5 K are found but the majority of solutions have central temperature in the range of the reference models. For $\beta = 0.1$, almost all central temperature solutions are in the range of the reference models and no solutions were found with central temperatures higher than $10^{4.6}$ K.

Table 5 shows the composition range for all β values 0.1, 0.5 and 1 split up into four different temperature model categories.

	reference temperature models	moderate models	hot models	extreme hot models
$\log T_c$ [K]	3.3 - 4.5	4.5 - 4.9	4.9 - 5.05	> 5.05
$\beta = 1$				
number of models	82	586	434	317
$H - He$	0.01 - 0.06	0.01 - 0.06	0.00 - 0.04	0.00 - 0.03
H_2O	0.62 - 0.92	0.28 - 0.92	0.02 - 0.40	0.01 - 0.25
SiO_2	0.00 - 0.30	0.00 - 0.67	0.26 - 0.92	0.01 - 0.92
Fe	0.00 - 0.03	0.00 - 0.03	0.00 - 0.36	0.00 - 0.86
$\beta = 0.5$				
number of models	964	73	138	70
$H - He$	0.01 - 0.08	0.00 - 0.07	0.00 - 0.02	0.00 - 0.03
H_2O	0.64 - 0.98	0.55 - 0.87	0.03 - 0.37	0.01 - 0.23
SiO_2	0.00 - 0.31	0.01 - 0.42	0.43 - 0.95	0.03 - 0.76
Fe	0.00 - 0.02	0.00 - 0.02	0.00 - 0.39	0.09 - 0.88
$\beta = 0.1$				
$H - He$	0.01 - 0.12			
H_2O	0.70 - 0.96			
SiO_2	0.00 - 0.30			
Fe	0.00 - 0.016			

Table 5: Total mass fractions overview for all components in different model categories for $\beta =$ 1, 0.5, 0.1

The choice of β has a great influence on the central temperature distribution of the solutions. The composition range mainly depends on the central temperature and not as much on the β value. If we only look at the composition ranges of only one central temperature category in many cases the range doesn't vary much for the different β values. We can use this recognition to make a summary of the composition range independent of the β choice. The total mass fraction range for $H - He$ and Fe for all temperature categories only varies slightly with a change of β. For H_2O and SiO_2, the composition range in some cases varies a bit more with a change of

β. Table 6 shows the whole composition range for different central temperature categories if all results for $\beta = 1, 0.5, 0.1$ are considered.

	reference temperature models	moderate models	hot models	extreme hot models
$\log T_c$ [K]	3.3 - 4.5	4.5 - 4.9	4.9 - 5.05	> 5.05
$H - He$	0.01 - 0.12	0.00 - 0.07	0.00 - 0.04	0.00 - 0.03
H_2O	0.62 - 0.98	0.28 - 0.92	0.02 - 0.40	0.01 - 0.25
SiO_2	0.00 - 0.31	0.00 - 0.67	0.26 - 0.95	0.01 - 0.92
Fe	0.00 - 0.03	0.00 - 0.03	0.00 - 0.39	0.00 - 0.88

Table 6: Total mass fractions summary for all components in different model categories for $\beta = 1, 0.5, 0.1$

The total mass fraction range of $H - He$ can be narrowed down the best since, independent of β and the central temperature, it is always in a range between 0 and 0.12. The total mass fraction ranges of H_2O and SiO_2 depend very much on the central temperatures. The lower the central temperatures are, the higher the total water and the lower the total rock mass fraction gets. For a central temperature range as in the reference models, the total mass fraction of rocks (SiO_2) is always below 0.31 and the total mass fraction of water, in this case, is between 0.62 and 0.98. For higher central temperatures the total water mass fraction can go down to 0.01 and the the total rock (SiO_2) mass fraction goes up to 0.95. The total iron mass fraction range depends very much on the central temperature. While for central temperature below $10^{4.9}$ K the total mass fraction is always below 0.03 it can get up to 0.88 for central temperatures higher than $10^{5.05}$ K. Such high total iron mass fractions are only found in a few solutions with very high central temperatures and don't seem realistic.

4.4 Discussion of composition layers

In this thesis, a broad variety of composition profiles were found. The composition profiles depend strongly on the density profiles used and the choice of β and/or the central temperature. In this section, the range of different composition profiles is shown and possible layer transitions are discussed. The profiles are split into different categories. In section 4.4.1 the compositions only containing hydrogen-helium and water are discussed. The profiles in section 4.4.2 contain hydrogen-helium, water and rocks (SiO_2). In section 4.4.3 the compositions containing hydrogen-helium, water, rocks (SiO_2) and iron are presented.

4.4.1 Compositions with hydrogen-helium and water

For a few profiles with $\beta = 0.1$ and $\beta = 0.5$, it is possible to find compositions that only contain hydrogen-helium and water. All those profiles look very similar to the example profile in figure 37. They start at the surface with a lower water mass fraction and have the strongest increase of water mass fraction in the radial range (0.7 - 1) r/R_{Uranus}. After this increase, many of those compositions remain constant or only have a small increase of water towards the center. For all of those Profiles, the $H - He$ mass fraction drops below 0.2 at a radius higher than 0.7 r/R_{Uranus}.

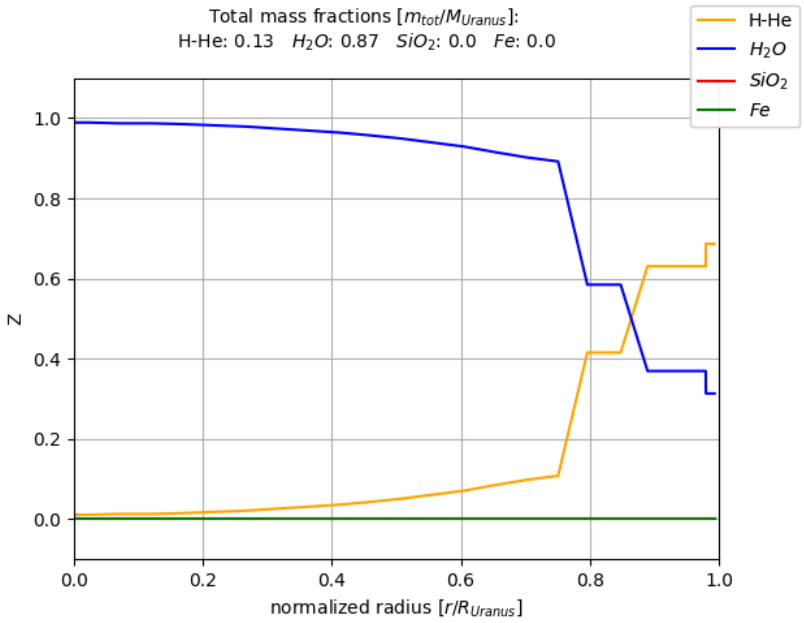

Figure 37: Possible $H - He$ and H_2O composition of density model 37 with $\beta = 0.1$

4.4.2 Compositions with hydrogen-helium, water and rocks (SiO_2)

Most of the profiles found with β values 1, 0.5 and 0.1 contain hydrogen-helium, water and rocks. In this section, different layer transitions found for this set of components are shown.

The most common profile type found for this combination of components is shown in figure 38. For this profile type the SiO_2 mass fraction continuously increases starting in a radial range between 0.2 and 0.8 r/R_{Uranus} and stays below a mass fraction of 0.5 in most cases. In some cases, a mass fraction jump closer to the center leads to SiO_2 mass fractions up to 1.

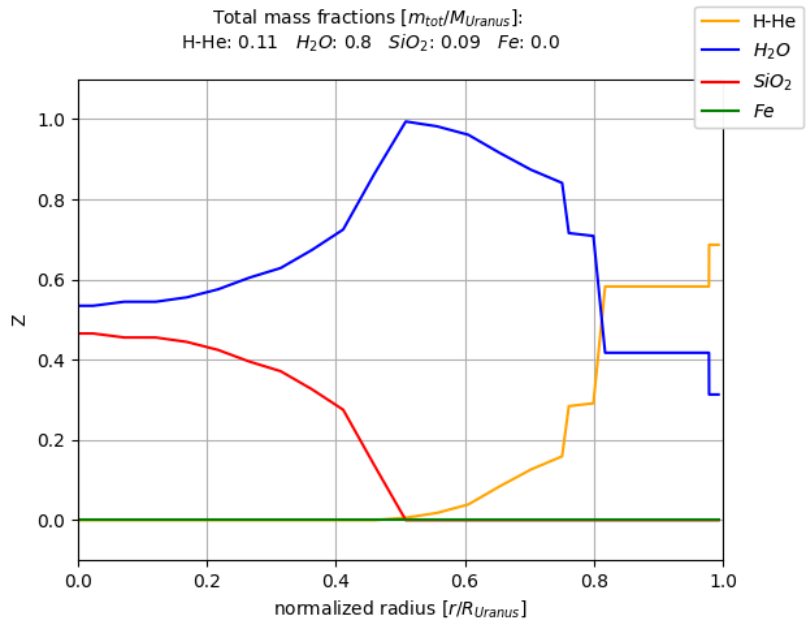

Figure 38: Possible $H-He$, H_2O, SiO_2 composition of density model 43 with $\beta = 0.5$

For $\beta = 1$ and $\beta = 0.5$ some solutions similar to the composition shown in figure 39 were found. Those profiles have their strongest increase of rocks in the radial range between 0.6 and 0.8 r/R_{Uranus} and usually reach SiO_2 mass fraction higher than 0.8 towards the center. Since by construction of the random walk algorithm, only mixtures of two materials can exist, the $H-He$ mass fraction in this profile type drops to 0 in the radial range between 0.6 and 0.8 r/R_{Uranus} and below 0.2 at a radius higher than 0.7 r/R_{Uranus}. For very few similar profiles the increase of SiO_2 already begins above 0.8 r/R_{Uranus}.

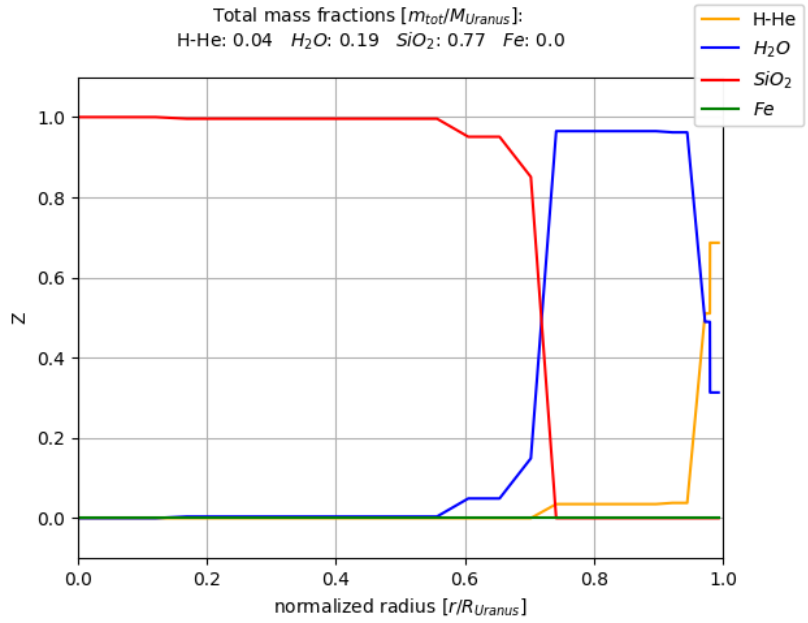

Figure 39: Possible $H-He$, H_2O, SiO_2 composition of density model 31 with $\beta = 1$

For $\beta = 0.1$ and $\beta = 0.5$ some solutions were found similar to the one shown in figure 40. In this profile type, there is a mass fraction jump of SiO_2 in the radial range between 0.7 and 0.8 r/R_{Uranus} and a drop to 0 of the $H-He$ mass fraction in the same range. After the jump both water and rocks mass fractions remain constant and the rocks (SiO_2) mass fraction stays below 0.5. In some cases, the water mass fraction remains relatively constant for the whole radial range while in others there is also an abrupt increase of the water mass fraction in the radial range between 0.7 and 0.8 r/R_{Uranus}.

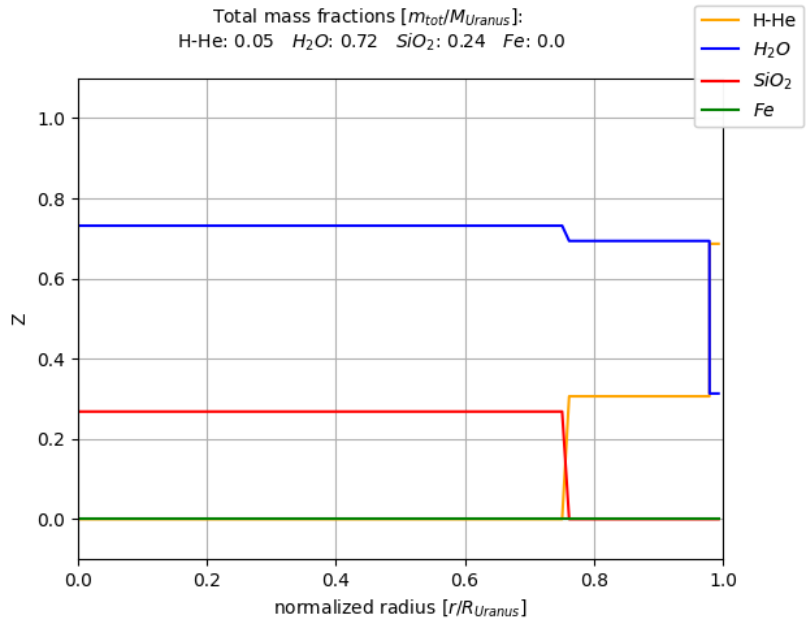

Figure 40: Possible $H-He$, H_2O, SiO_2 composition of density model 34 with $\beta = 0.1$

For $\beta = 1,\ 0.5,\ 0.1$ some solutions were found similar to the one shown in figure 41. In this profile type, there is a mass fraction jump of SiO_2 in the radial range between 0.1 and 0.4 r/R_{Uranus} and a drop of the H_2O mass fraction in the same range. After the jump, the rocks (SiO_2) mass fraction reaches values above 0.5. The $H-He$ mass fraction already drops below 0.2 at a radius higher than 0.7 r/R_{Uranus}.

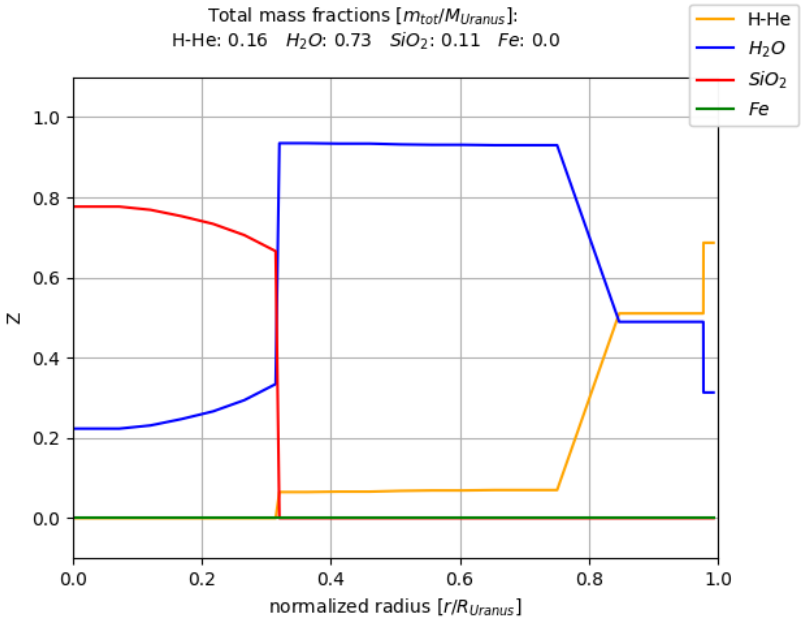

Figure 41: Possible $H-He$, H_2O, SiO_2 composition of density model 63 with $\beta = 0.1$

For the composition profiles that are composed of hydrogen-helium, water and rocks (SiO_2) we can get very different solutions. However, there are some properties that they all have in common. For all profiles, the $H-He$ mass fraction drops below 0.2 and the H_2O mass fraction increases to a value above 0.6 at a radius higher than 0.7 r/R_{Uranus}.

4.4.3 Compositions with hydrogen-helium, water, rocks (SiO_2) and iron

For some profiles with $\beta = 1,\ 0.5,\ 0.1$ compositions containing hydrogen-helium, water, rocks and iron are found. In this section, different layer transitions found for this set of components are shown.

The most common profile type found for this combination of components is shown in figure 42a. For this profile type the SiO_2 mass fraction increases slowly starting in a radial range between 0.2 and 0.8 r/R_{Uranus}. In the radial range below 0.2 r/R_{Uranus} the water mass fraction drops instantaneously to zero and the iron makes a jump from zero to any mass fraction between 0.05 and 1. At the same radius where we observe the iron jump there is usually also a jump of the SiO_2 mass fraction from values below 0.5 to any value between 0 and 1. In most cases, the jump leads to an increase in mass fraction as shown in figure 42a while in some cases the jump leads to a decrease of the SiO_2 mass fraction. The $H-He$ mass fraction drops below 0.1 in at a radius higher than 0.7 r/R_{Uranus}. For $\beta = 0.1$ profiles like the example shown in figure 42b are more common. This type of profile shares most of the described properties with the profile type shown in figure 42a. The only difference is that in this profile type the SiO_2 mass fraction stays zero until the jump in the region below 0.2 r/R_{Uranus}.

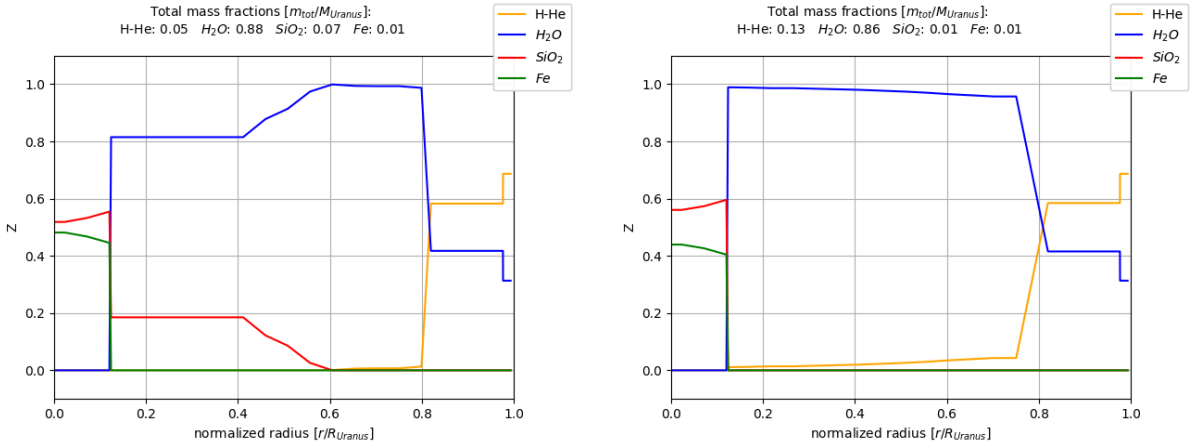

(a) With $\beta = 0.5$ (b) With $\beta = 0.1$

Figure 42: Compositions with $H - He$, H_2O, SiO_2 and Fe of density model 84

For $\beta = 0.5$ and $\beta = 1$ some profiles with very high central temperatures are found similar to the example shown in figure 43. This type of profile has an iron mass fraction gradually increasing to values above 0.8 in the region between 0.2 and 0.8 r/R_{Uranus}. The $H - He$ mass fractions in these profiles drop below 0.2 in the region above 0.8 r/R_{Uranus}.

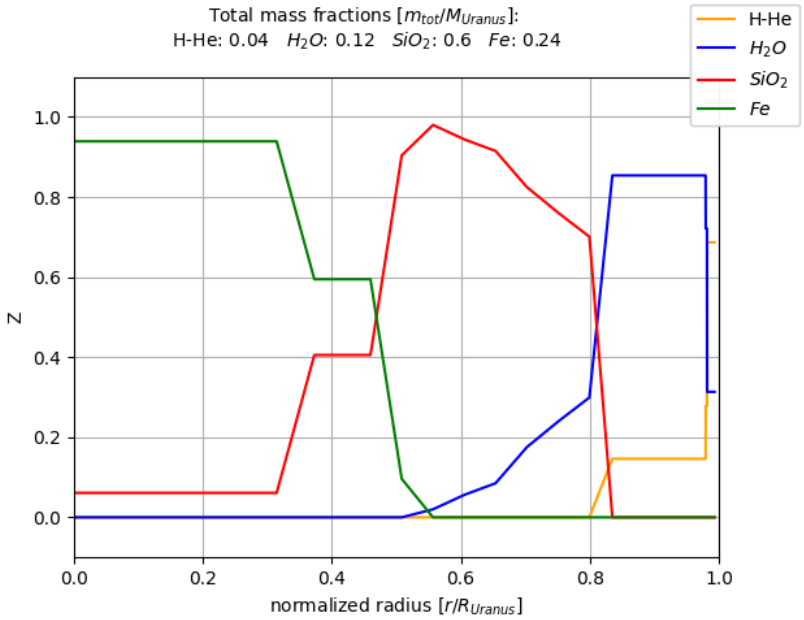

Figure 43: Possible $H - He$, H_2O, SiO_2, Fe composition of density model 49 with $\beta = 1$

For $\beta = 1$, some profiles similar to the example shown in figure 43 are found. In this type of profiles, a fast increase of the SiO_2 mass fraction happens between 0.6 and 0.9 r/R_{Uranus} reaching values above 0.8 after the increase. In a region below 0.4 r/R_{Uranus} a jump of iron raises the iron mass fraction to values between 0.1 and 1. The $H - He$ mass fraction drops below 0.2 in a region above 0.8 r/R_{Uranus}.

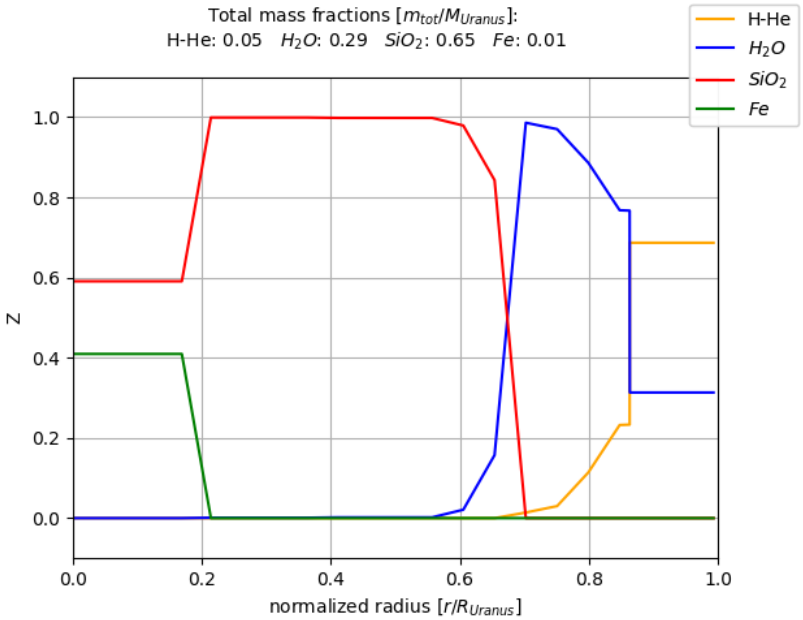

Figure 44: Possible $H-He$, H_2O, SiO_2, Fe composition of density model 54 with $\beta = 1$

For the composition profiles that are composed of hydrogen-helium, water, rocks (SiO_2) and iron we can get very different solutions. However, there are some properties that they all have in common. For all profiles, the $H-He$ mass fraction drops below 0.2 and the H_2O mass fraction increases to a value above 0.8 at a radius higher than 0.7 r/R_{Uranus}.

5 Conclusions & Outlook

Conclusions

In this thesis, we presented a random walk approach to derive temperature and composition models for Uranus based on a density profile. The temperature profiles in this thesis tend to be higher than the temperature models of prior publications from Nettelmann et al., Podolak et al., Neuenschwander et al.. The height of the temperature profiles depends much on the limit β from equation 19 on the temperature gradient. In some cases choosing a small enough β value can limit the temperature solution such that they are in the range of prior publications. However in other cases for smaller β values no solutions could be found. The best agreement of temperature profiles from this thesis and prior publications was found for the temperature models U1 and U2 from [13] and the models 2 PV and 4 PV from [15].

In the analysis of the temperature profiles based on the density profiles from Luca Morf, we investigated the central temperature ranges. With no limit on the temperature gradient ($\beta = 1$), the central temperatures are in a range $T_c = (1.1 - 16.5) \cdot 10^4$ K. With lower temperature gradient limits such as $\beta = 0.1$ the central temperatures can also be limited to a lower range $T_c = (0.4-4)\cdot 10^4$ K. For $\beta = 0.5$ the central temperatures are in the range $T_c = (0.8-16.5)\cdot 10^4$. For many profiles from figure 4b we were able to find profiles with adiabatic solutions in the ionic water region. This profile structure could form a dynamo allowing the creation of a magnetic field. If we only consider the dynamo consistent profiles and apply no temperature gradient limit ($\beta = 1$), the central temperatures can be limited to a more narrow spectrum of $T_c = (1.7-11.3)\cdot 10^4$ K. For the lower temperature gradient limit $\beta = 0.1$ the central temperature range remains $T_c = (0.4-4)\cdot 10^4$ K regardless of whether all profiles or only the dynamo consistent profiles are considered. For $\beta = 0.5$, the dynamo consistent profiles have a central temperature range of $T_c = (1.4 - 3.7) \cdot 10^4$ K if outliers are neglected. Our total mass fraction solutions of a profile from figure 4b have a strong dependence on the central temperature of the profile. Therefore the profiles from section 4.2 were split up into four categories: "reference temperature model", "moderate model", "hot model" and "extreme hot model". Table 7 shows the ranges of total mass fractions for all β choices and split up into the four temperature categories.

	reference temperature models	moderate models	hot models	extreme hot models
$\log T_c$ [K]	3.3 - 4.5	4.5 - 4.9	4.9 - 5.05	> 5.05
$H - He$	0.01 - 0.12	0.00 - 0.07	0.00 - 0.04	0.00 - 0.03
H_2O	0.62 - 0.98	0.28 - 0.92	0.02 - 0.40	0.01 - 0.25
SiO_2	0.00 - 0.31	0.00 - 0.67	0.26 - 0.95	0.01 - 0.92
Fe	0.00 - 0.03	0.00 - 0.03	0.00 - 0.39	0.00 - 0.88

Table 7: Total mass fractions summary for all components in different model categories for $\beta = 1, 0.5, 0.1$

Independent of the central temperature the total mass fraction of hydrogen-helium was below 0.12 for all our composition solutions for the density profiles from figure 4b and all gradient limits $\beta = 0.1, 0.5, 1$. For the composition layers, we found a broad variety of solutions with most profiles containing hydrogen-helium, water and rocks (SiO_2). Some profiles are composed of hydrogen-helium, water, rocks (SiO_2) and iron and a few profiles only contain hydrogen-helium and water. Independent of the compositions all profiles have in common that the hydrogen-helium mass fraction drops below 0.2 at a radius higher than 0.7 r/R_{Uranus}. And the water mass fraction increases to a value above 0.6 at a radius higher than 0.7 r/R_{Uranus}.

Outlook

Some aspects of the composition and the temperature result are strongly influenced by the construction of the random walk algorithm. It is important to note that the random walk algorithm as presented in this thesis only allows mixtures of two materials. This has a great impact on the composition and the total mass fractions of the components. The total mass fraction of hydrogen-helium is limited to a lower value by construction of the random walk algorithm since in the interior as soon as rock is present the algorithm doesn't allow the presence of hydrogen-helium anymore. For future work, it would be interesting to consider also mixtures of more than two components.

The height of the temperature solution depends strongly on the temperature gradient limit β from equation 19. The values for β in this thesis were arbitrarily selected, as there is no theoretical basis guiding their choice. The values were chosen such that they reflect a range of possible profiles for different β values but it is crucial to approach the choices and their corresponding temperature solutions with caution.

To compatibility of the solutions with magnetic field generation depends on the presence of an adiabatic profile in the ionic water region. It is important to note that the ionic water region, used in this thesis was derived for pure water while the profile solutions in this thesis aren't composed of pure water in this region. The ionic region has already an uncertainty of 10-20% for pure water. For a mixture of water and additional elements, we don't know how accurate this region still is. The presence of an adiabatic region depends on the choice of the relative entropy change variable ϵ in equation 18.

Although the choices we make for the gradient limit β and the entropy change variable ϵ influence our solutions, the density profile we use usually has a greater impact on the composition solutions. A mission dedicated to measuring Uranus' gravitational field with a higher accuracy would help constrain the density profiles and therefore would also further constrain the composition profiles.

References

[1] M. Bethkenhagen, E. R. Meyer, S. Hamel, N. Nettelmann, M. French, L. Scheibe, C. Ticknor, L. A. Collins, J. D. Kress, J. J. Fortney, and R. Redmer. Planetary ices and the linear mixing approximation. *The Astrophysical Journal*, 848(1):67, oct 2017. doi: 10.3847/1538-4357/aa8b14. URL https://dx.doi.org/10.3847/1538-4357/aa8b14.

[2] G. Chabrier, S. Mazevet, and F. Soubiran. A new equation of state for dense hydrogen–helium mixtures. *The Astrophysical Journal*, 872(1):51, feb 2019. doi: 10.3847/1538-4357/aaf99f. URL https://dx.doi.org/10.3847/1538-4357/aaf99f.

[3] P. Garaud. Double-diffusive convection at low prandtl number. *Annual Review of Fluid Mechanics*, 50(1):275–298, 2018. doi: 10.1146/annurev-fluid-122316-045234. URL https://doi.org/10.1146/annurev-fluid-122316-045234.

[4] J. Haldemann, Y. Alibert, C. Mordasini, and W. Benz. AQUA: a collection of h2o equations of state for planetary models. 643:A105. ISSN 0004-6361, 1432-0746. doi: 10.1051/0004-6361/202038367. URL https://www.aanda.org/articles/aa/abs/2020/11/aa38367-20/aa38367-20.html. Publisher: EDP Sciences.

[5] R. Helled and J. J. Fortney. The interiors of Uranus and Neptune: current understanding and open questions. *Philosophical Transactions of the Royal Society A: Mathematical, Physical and Engineering Sciences*, 378(2187):20190474, Nov. 2020. doi: 10.1098/rsta.2019.0474. URL https://royalsocietypublishing.org/doi/10.1098/rsta.2019.0474. Publisher: Royal Society.

[6] R. Helled, J. D. Anderson, M. Podolak, and G. Schubert. INTERIOR MODELS OF URANUS AND NEPTUNE. *The Astrophysical Journal*, 726(1):15, dec 2010. doi: 10.1088/0004-637x/726/1/15. URL https://doi.org/10.1088%2F0004-637x%2F726%2F1%2F15.

[7] R. Helled, N. Nettelmann, and T. Guillot. Uranus and neptune: Origin, evolution and internal structure. *Space Science Reviews*, 216(3), mar 2020. doi: 10.1007/s11214-020-00660-3. URL https://doi.org/10.1007%2Fs11214-020-00660-3.

[8] R. Kippenhahn, A. Weigert, and A. Weiss. *Stellar Structure and Evolution*. Astronomy and Astrophysics Library. Springer, Berlin, Heidelberg, 2012. ISBN 978-3-642-30255-8 978-3-642-30304-3. doi: 10.1007/978-3-642-30304-3. URL http://link.springer.com/10.1007/978-3-642-30304-3.

[9] K. Lodders. Solar elemental abundances, 2019.

[10] U. Malamud and D. Prialnik. Modeling kuiper belt objects charon, orcus and salacia by means of a new equation of state for porous icy bodies. *Icarus*, 246:21–36, 2015. ISSN 0019-1035. doi: https://doi.org/10.1016/j.icarus.2014.02.027. URL https://www.sciencedirect.com/science/article/pii/S0019103514001134. Special Issue: The Pluto System.

[11] R. M. More, K. H. Warren, D. A. Young, and G. B. Zimmerman. A new quotidian equation of state (QEOS) for hot dense matter. *Physics of Fluids*, 31(10):3059–3078, Oct. 1988. doi: 10.1063/1.866963.

[12] N. F. Ness, M. H. Acuña, K. W. Behannon, L. F. Burlaga, J. E. P. Connerney, R. P. Lepping, and F. M. Neubauer. Magnetic fields at uranus. *Science*, 233(4759):85–89, 1986. doi: 10.

1126/science.233.4759.85. URL https://www.science.org/doi/abs/10.1126/science.233.4759.85.

[13] N. Nettelmann, R. Helled, J. J. Fortney, and R. Redmer. New indication for a dichotomy in the interior structure of Uranus and Neptune from the application of modified shape and rotation data. *Planetary and Space Science*, 77:143–151, 2013. ISSN 0032-0633. doi: https://doi.org/10.1016/j.pss.2012.06.019. URL https://www.sciencedirect.com/science/article/pii/S0032063312001900.

[14] B. A. Neuenschwander and R. Helled. Empirical structure models of Uranus and Neptune. *Monthly Notices of the Royal Astronomical Society*, 512(3):3124–3136, Mar. 2022. ISSN 0035-8711, 1365-2966. doi: 10.1093/mnras/stac628. URL https://academic.oup.com/mnras/article/512/3/3124/6546168.

[15] B. A. Neuenschwander, S. Müller, and R. Helled. Uranus' complex internal structure. *A&A*, submitted, 2024.

[16] B. Paxton, M. Cantiello, P. Arras, L. Bildsten, E. F. Brown, A. Dotter, C. Mankovich, M. H. Montgomery, D. Stello, F. X. Timmes, and R. Townsend. Modules for Experiments in Stellar Astrophysics (MESA): Planets, Oscillations, Rotation, and Massive Stars. , 208 (1):4, Sept. 2013. doi: 10.1088/0067-0049/208/1/4.

[17] J. I. Podolak, U. Malamud, and M. Podolak. Random models for exploring planet compositions i: Uranus as an example. *Icarus*, 382:115017, 2022. ISSN 0019-1035. doi: https://doi.org/10.1016/j.icarus.2022.115017. URL https://www.sciencedirect.com/science/article/pii/S0019103522001312.

[18] M. Podolak, R. Helled, and G. Schubert. Effect of non-adiabatic thermal profiles on the inferred compositions of Uranus and Neptune. , 487(2):2653–2664, Aug. 2019. doi: 10.1093/mnras/stz1467.

[19] R. Redmer, T. R. Mattsson, N. Nettelmann, and M. French. The phase diagram of water and the magnetic fields of uranus and neptune. *Icarus*, 211(1):798–803, 2011. ISSN 0019-1035. doi: https://doi.org/10.1016/j.icarus.2010.08.008. URL https://www.sciencedirect.com/science/article/pii/S0019103510003143.

[20] D. Saumon, G. Chabrier, and H. M. van Horn. An Equation of State for Low-Mass Stars and Giant Planets. , 99:713, Aug. 1995. doi: 10.1086/192204.

[21] S. Stanley and J. Bloxham. Numerical dynamo models of uranus' and neptune's magnetic fields. *Icarus*, 184(2):556–572, 2006. ISSN 0019-1035. doi: https://doi.org/10.1016/j.icarus.2006.05.005. URL https://www.sciencedirect.com/science/article/pii/S0019103506001680.

[22] E. C. Stone and E. D. Miner. The voyager 2 encounter with the uranian system. *Science*, 233(4759):39–43, 1986. doi: 10.1126/science.233.4759.39. URL https://www.science.org/doi/abs/10.1126/science.233.4759.39.